

## GALAXIES IN THE FIELDS OF $z \sim 1.5$ RADIO-LOUD QUASARS

PATRICK B. HALL,<sup>1,2,3,4,5</sup> MARCIN SAWICKI,<sup>6</sup> PAUL MARTINI,<sup>7,8</sup> ROSE A. FINN,<sup>9</sup> C. J. PRITCHET,<sup>10,11</sup> PATRICK S. OSMER,<sup>7</sup>  
DONALD W. MCCARTHY,<sup>9</sup> AARON S. EVANS,<sup>4,6,12</sup> HUAN LIN,<sup>3,9,12</sup> AND F. D. A. HARTWICK<sup>3,10</sup>

Received 2000 November 19; accepted 2000 December 27

### ABSTRACT

We have previously identified an excess population of predominantly red galaxies around a sample of 31 radio-loud quasars (RLQs) at  $1 < z < 2$ . Here we show that these fields have a surface density of extremely red objects (EROs, with  $R-K > 6$ ) 2.7 times higher than the general field. Assuming these EROs are passively evolved galaxies at the quasar redshifts, they have characteristic luminosities of only  $\sim L^*$ . Only one of four RLQ fields has an excess of  $J-K$ -selected EROs with  $J-K > 2.5$ ; thus, those objects are mostly unrelated to the quasars. We also present new multiwavelength data and analyses on the fields of four of these quasars at  $z_q \sim 1.54$ , obtained to build more detailed pictures of the environments of these quasars and the galaxies within them. First, wide-field  $J$  and  $K_s$  data show that the galaxy excess around Q0835+580 is of Abell richness  $2 \pm 1$  and extends to  $140''$  and that the galaxy excess around Q1126+101 extends to only  $50''$ , even though the overall counts in the field are higher than the literature average. Second, in three fields we present the deepest narrowband redshifted  $H\alpha$  observations yet published. We detect five candidate galaxies at the quasar redshifts, a surface density 2.5 times higher than in the only existing random-field survey of similar depth. However, photometric spectral energy distribution (SED) fitting of one candidate suggests that it is an [O III] detection background to the quasar. Third, SCUBA submillimeter observations of three fields detect two of the quasars and two galaxies with SEDs best fitted as highly reddened galaxies at the quasar redshifts. Fourth,  $H$ -band adaptive optics (AO) imaging is used to estimate redshifts for two moderately red bulge-dominated galaxies in the Q0835+580 field using the Kormendy relation between central surface brightness and half-light radius. Both have structural redshifts consistent with early-type galaxies foreground to the quasar at  $z \lesssim 0.2$  or  $1 \lesssim z \lesssim 1.35$ . Photometric redshifts do not confirm these structural redshifts, however, possibly because our optical photometry for these objects is corrupted by scattered light from the nearby bright AO guide star. Finally, quantitative SED fits are presented for numerous galaxies of interest in two fields and are used to constrain their photometric redshifts,  $z_{\text{ph}}$ . Most galaxies in the spatially compact group around Q0835+580 are consistent with being at the quasar redshift  $z_q$ . One of these is a candidate very old galaxy without ongoing star formation, while the others appear to have ongoing or recent star formation. Many very and extremely red objects across both fields have  $z_{\text{ph}} \simeq z_q$ , and significant dust is required to fit most of them, including about half of the objects whose fits also require relatively old stellar populations. Large reddenings of  $E(B-V) \simeq 0.6 \pm 0.3$  are also required to fit four  $J-K$ -selected EROs in the Q1126+101 field, though all but one of them have best-fit redshifts  $z_{\text{ph}} > z_q$ . These objects may represent a population of dusty high-redshift galaxies underrepresented in optically selected samples.

Taken together, these observations reinforce the claim that radio-loud quasars at  $z_q > 1$  can be found in galaxy overdensities. Ongoing star formation with moderate amounts of dust seems to be common among all but the very reddest galaxies in these overdensities.

*Key words:* galaxies: clusters: general — galaxies: general —  
quasars: individual (Q0835+580, Q1126+101, Q2149+212, Q2345+061) —  
infrared radiation

*On-line material:* color figures

<sup>1</sup> Department of Astronomy, University of Toronto, 60 St. George Street, Toronto, ON M5S 3H8, Canada.

<sup>2</sup> Now at Princeton University Observatory, Princeton, NJ 08544-1001, and Pontificia Universidad Católica de Chile, Departamento de Astronomía y Astrofísica, Facultad de Física, Casilla 306, Santiago 22, Chile; phall@astro.puc.cl

<sup>3</sup> Visiting Astronomer, Canada-France-Hawaii Telescope, operated by the National Research Council of Canada, the Centre National de la Recherche Scientifique de France, and the University of Hawaii.

<sup>4</sup> Visiting Astronomer, James Clerk Maxwell Telescope, operated by The Joint Astronomy Centre on behalf of the Particle Physics and Astronomy Research Council of the United Kingdom, the Netherlands Organisation for Scientific Research, and the National Research Council of Canada.

<sup>5</sup> Visiting Astronomer, Infrared Telescope Facility, operated by the University of Hawaii under contract to the National Aeronautics and Space Administration.

<sup>6</sup> California Institute of Technology, Mail Stop 320-47, Pasadena, CA 91125.

<sup>7</sup> Department of Astronomy Department, Ohio State University, 140 West 18th Avenue, Columbus, OH 43210-1173.

<sup>8</sup> Current address: Carnegie Observatories, 813 Santa Barbara Street, Pasadena, CA 91101.

<sup>9</sup> Steward Observatory, University of Arizona, Tucson, AZ 85721.

<sup>10</sup> Department of Physics and Astronomy, University of Victoria, Victoria, BC V8W 3P6, Canada.

<sup>11</sup> Current address: Department of Physics and Astronomy, State University of New York at Stony Brook, Stony Brook, NY 11794-3800.

<sup>12</sup> Hubble Fellow.

## 1. INTRODUCTION

It is of considerable current interest to efficiently identify clusters and other concentrations of galaxies at  $z > 1$  in order to study the evolution of both galaxies and large-scale structure. Radio-loud quasars (RLQs) are among the obvious signposts around which to search for clusters at  $z > 1$ . This is because RLQs almost exclusively reside in giant elliptical galaxies (a strongly clustered population) and some RLQs have been spectroscopically confirmed to inhabit clusters at  $z \lesssim 0.7$  (Yee & Ellingson 1993). In Hall, Green, & Cohen (1998), hereafter HGC98, and Hall & Green (1998), hereafter HG98, we presented optical ( $r \lesssim 25.5$ ) and near-IR ( $K \lesssim 21$ ) imaging of the fields of 31 RLQs at  $1 < z < 2$  which revealed an excess of predominantly red galaxies at  $K > 19$ . The excess has two spatial components—one within  $40''$  of the quasars and one extending out to at least  $\sim 2'$ —consistent with the quasars often residing in galaxy groups or poor clusters which are themselves found within richer filaments or sheets of galaxies. The images of HGC98 were at most  $3' \times 3'$  in size, and so could only place a lower limit on the size of the large-scale galaxy excess (relative to blank-field galaxy counts at these magnitudes) around the quasars. The magnitude and color distributions of the excess galaxies are consistent with a population of predominantly early-type galaxies at the quasar redshifts. However, a possible exception is some or all of the  $J$ -band dropouts ( $J-K > 2.5$ ) found in five fields for which we have  $J$  imaging. Such very red  $J-K$  colors require that the galaxies are reddened by dust or are at  $z \gtrsim 2.5$  so that the  $4000 \text{ \AA}$  break lies beyond the  $J$  band, or both.

Spectroscopic confirmation of overdensities at the quasar redshifts in these RLQ fields is still lacking, as are spectroscopic redshifts for the  $J$ -band dropouts, because of the difficulty of obtaining spectroscopic redshifts for galaxies at  $1.5 \lesssim z \lesssim 2.5$ , and extremely red galaxies at all  $z \gtrsim 1$ . To provide a more comprehensive picture of these systems in the absence of spectroscopy, in this paper we present further analyses of the excess galaxy population as well as various new observations of four of these RLQ fields. The results reported here supersede earlier results reported as work in progress in Hall et al. (1999) and Hall, Sawicki, & Lin (2000). In § 2 we present new wide-field near-IR imaging and study the extent of the galaxy overdensities. In § 3 we discuss the surface density of extremely red objects (EROs) in these RLQ fields compared with field surveys. In § 4 we present narrowband imaging sensitive to  $H\alpha$  emission from galaxies at the quasar redshifts. In § 5 we present sub-millimeter mapping sensitive to dust in luminous star-forming galaxies. In § 6 we present adaptive-optics imaging of two galaxies. In § 7 we present multicolor SED fits used to derive photometric redshifts, reddenings, and age estimates for selected galaxies. We summarize our results in § 8. We adopt a  $\Lambda = 0$  cosmology with  $H_0 = 75 \text{ km s}^{-1} \text{ Mpc}^{-1}$  and  $q_0 = 0.1$  (for a projected scale of  $7.4 h_{75} \text{ kpc arcsec}^{-1}$  at  $z = 1.54$ ), except as noted for comparison with the literature.

## 2. WIDE-FIELD NEAR-IR IMAGING

We obtained  $J$  and  $K_s$  data over wider fields around two RLQs from HGC98 to help verify the reality of the large-scale galaxy excess and to search for additional  $J$ -band dropouts. Information about these RLQs, the two other

RLQs studied in this paper, and the observations obtained in the field of each is given in Table 1. The near-IR imaging data were reduced using PHIIRS.<sup>13</sup> Standard infrared observing and reduction procedures were used, including flattening using either dome flats or “running sky flats” created from the science images themselves. Object detection and photometry using FOCAS (Valdes 1982)<sup>14</sup> followed the procedure of HGC98.

## 2.1. Q0835 + 580 Field Observations and Reductions

We obtained  $J$  and  $K_s$  data over a  $\sim 9'$  diameter unvignetted field of view at plate scale  $0''.5 \text{ pixel}^{-1}$  at the Steward Observatory  $90''$  telescope with PISCES (McCarthy et al. 1998; McCarthy et al. 2000), which incorporates a  $1024^2$  HgCdTe detector. PISCES has significant optical distortions in both  $J$  and  $K_s$  which must be removed before co-adding. Observations of M67 (Girard et al. 1989) were used to calculate distortion solutions for the 1999 April run, yielding images oriented to true north and east (as defined by the USNOA-2.0 catalog) to within  $\leq 0.12$  accuracy.

Calibration used ARNICA (Hunt et al. 1998) and NICMOS (Persson et al. 1998) standards and assumed extinction coefficients of 0.08 in  $J$  and 0.07 in  $K_s$ . Both object detection and aperture definition were done on the summed  $J+K_s$  image (total area  $52.561 \text{ arcmin}^2$ ), and FOCAS total magnitudes were produced using those same apertures on the  $J$  and  $K_s$  images.

## 2.2. Q1126 + 101 Field Observations and Reductions

We imaged Q1126 + 101 with the near-infrared imager/spectrograph TIFKAM (a.k.a. ONIS at Kitt Peak; Pogge et al. 1998) at the 2.4 m Hiltner telescope of the MDM Observatory. TIFKAM has a  $512 \times 1024$  InSb array with a plate scale of  $0''.3 \text{ pixel}^{-1}$  at the 2.4 m, corresponding to a  $2.5' \times 5'$  field of view. We observed a field centered  $80''$  west of the quasar (which includes the quasar near the eastern edge of the array) in  $J$  and  $K_s$  in nonphotometric conditions of  $\sim 1''.5$  seeing. The co-added images were trimmed to the region of maximum exposure time ( $12.051 \text{ arcmin}^2$ ). The final  $J$  and  $K_s$  images completely overlap the  $r$ -band data of HGC98 and partially overlap the  $J$  and  $K_s$  data of HGC98. We rotated and magnified our new near-infrared observations to match those images and then catalogued all the objects in the sum of the  $r$  image and our new  $J$  and  $K_s$  images. Finally, we calibrated our  $J$  and  $K_s$  images using the objects in common with HGC98.

## 2.3. Wide-Field Near-IR Imaging Results

The  $K < 20.5$  galaxy surface density is  $17.5 \pm 0.6 \text{ arcmin}^{-2}$  in the Q0835 + 580 field and  $20.7 \pm 1.3 \text{ arcmin}^{-2}$  in the Q1126 + 101 field. These values are respectively 2.4 and 3.5  $\sigma$  above the literature compilation value of  $13.7 \pm 1.5$  (including rms field-to-field scatter) from HG98. Both values agree within 1.3  $\sigma$  with those measured in HGC98 using smaller ( $\sim 3' \times 3'$ ) images of these fields. The

<sup>13</sup> PHIIRS is Pat Hall's Infrared Imaging Reduction Software (Hall, Green, & Cohen 1998), a package of IRAF routines available from the first author or the IRAF contributed software Web site. The Image Reduction and Analysis Facility (IRAF) is distributed by the National Optical Astronomy Observatories, which is operated by the Association of Universities for Research in Astronomy, Inc., under contract to the National Science Foundation.

<sup>14</sup> Available at <http://iraf.noao.edu/iraf/docs/focas>.

TABLE 1  
OBSERVATIONS

Quasar	Q0835+580	Q1126+101	Q2149+212	Q2345+061
R.A. (J2000.0) .....	08 39 06.459	11 29 14.19	21 51 45.874	23 48 31.836
Decl. (J2000.0) .....	+57 54 17.12	+09 51 59.6	+21 30 13.51	+06 24 59.25
Redshift .....	$1.5358 \pm 0.0006$	$1.5173 \pm 0.0010$	$1.5385 \pm 0.0008$	$1.5396 \pm 0.0012$
Wide-Field Observations				
Telescope + instrument .....	SO 2.3 m + PISCES	MDM 2.4 m + TIFKAM	...	...
<i>J</i> date .....	1999 Jan 6	1999 Apr 6	...	...
<i>J</i> exposure .....	10560	10560	...	...
<i>J</i> 3 $\sigma$ limit .....	22.51	22.37	...	...
<i>K<sub>s</sub></i> date .....	1998 Sep 30, 1999 Apr 27–28	1999 Apr 7	...	...
<i>K<sub>s</sub></i> exposure .....	8980	12360	...	...
<i>K<sub>s</sub></i> 3 $\sigma$ limit .....	20.63	21.03	...	...
Narrowband H $\alpha$ Observations				
Telescope + instrument .....	IRTF + NSFCAM	...	CFHT + REDEYE	IRTF + NSFCAM; CFHT + REDEYE
Date .....	1997 Mar 19, Oct 26–30, Nov 1	...	1993 Sep 9	1997 Oct 26–30, Nov 1; 1993 Sep 9
Filter $\lambda$ ( $\mu$ m) .....	1.6549–1.6734	...	1.6631–1.6693	1.6574–1.6759; 1.6631–1.6693
<i>H</i> -band exposure .....	7920	...	810	5940; 570
H $\alpha$ exposure .....	34620	...	4200	37440; 7200
Area .....	0.926	...	3.982	0.697; 4.551
$f_{H\alpha}$ 3 $\sigma$ limit <sup>a</sup> .....	1.71	...	0.78	1.92; 0.87
JCMT + SCUBA Observations				
Date .....	1999 Mar 26	1999 Mar 25–26	...	1998 July 23
Exposure .....	7040	15360	...	10240
$\tau_{CSO}$ .....	0.02–0.08	0.02–0.07	...	0.055
rms noise at 850 $\mu$ m .....	2.21 mJy beam <sup>-1</sup>	1.83 mJy beam <sup>-1</sup>	...	4.2 mJy beam <sup>-1</sup>
CFHT PUEO + KIR <i>H</i> -band Adaptive Optics Observations				
Date .....	1999 Dec 30–31	...	...	...
Exposure .....	10350	...	...	...

NOTES.—Units of right ascension are hours, minutes, and seconds, and units of declination are degrees, arcminutes, and arcseconds. Redshifts are from the detailed study of Tytler & Fan (1992), except for Q1126+101, which was computed using their method. All observation dates are UT. All exposure times are in seconds. All areas are in arcmin<sup>2</sup>.  
<sup>a</sup> Units of 10<sup>-17</sup> ergs cm<sup>-2</sup> s<sup>-1</sup>.

*J* < 21.5 galaxy surface density is  $11.8 \pm 0.5$  arcmin<sup>-2</sup> in the Q0835+580 field and  $14.2 \pm 1.1$  arcmin<sup>-2</sup> in the Q1126+101 field. These values are slightly higher than the *J*-band field galaxy counts of Teplitz, McLean, & Malkan

(1999) and > 3  $\sigma$  higher than those of Saracco et al. (1999). Thus these new wide-field observations confirm that the surface density of faint *J*- and *K*-selected galaxies is higher in these RLQ fields than in random fields.

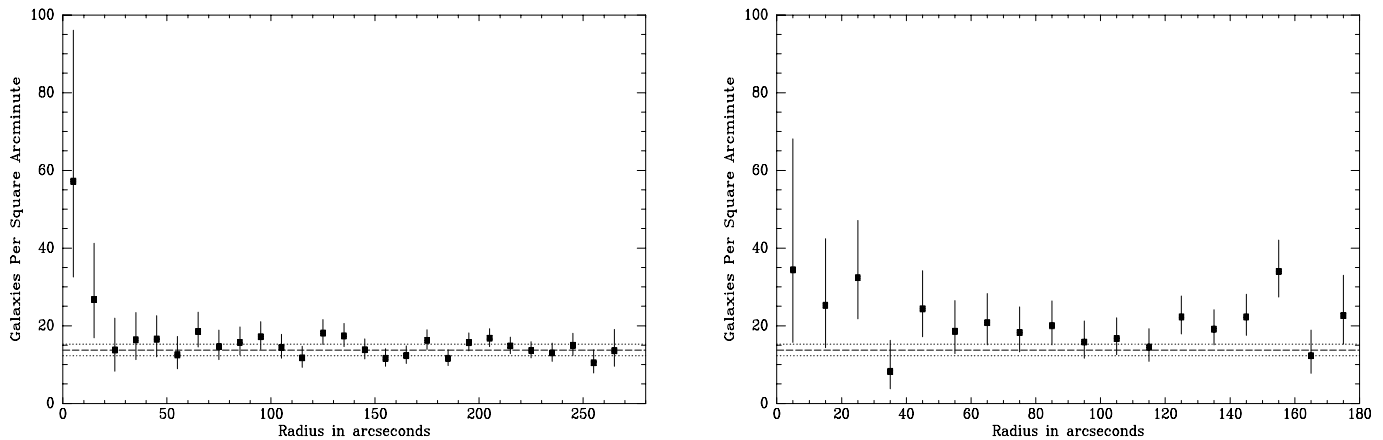


FIG. 1.—Radial distributions of all *K* < 20.5 galaxies relative to the two quasars with new wide-field *JK* imaging, plotted as points with error bars from Gehrels (1986). The average *K* < 20.5 counts and  $\pm 1 \sigma$  rms scatter from the literature data compiled in Hall & Green (1998) are plotted as dashed and dotted lines, respectively. *Left*: Q0835+580 field. There is a clear galaxy excess at  $< 20''$ . The overdensity on larger scales appears to extend out to  $\sim 140''$  at 2.35  $\sigma$  significance. *Right*: Q1126+101 field. There is an excess on all scales relative to the literature but only a weak excess at  $\lesssim 50''$  around the quasar relative to the counts in this field. The spike at  $\sim 150''$  is due to a galaxy grouping on the sky, which by chance is aligned tangentially to the quasar.

The radial distribution of all  $K < 20.5$  galaxies relative to Q0835+580 (Fig. 1a) shows a clear excess at  $< 20''$ . There also appears to be an overdensity extending out to  $\sim 140''$  ( $\sim 2 h_{75}^{-1}$  Mpc). From the surface density at  $> 140''$ , we would expect 245 galaxies within  $140''$  of the quasar. We observe 285, which is a  $2.35 \sigma$  excess. The radial distribution of all  $K < 20.5$  galaxies relative to Q1126+101 (Fig. 1b) shows a constant surface density within the uncertainties to  $180''$ , apart from a weak excess at  $\lesssim 50''$ .

Given this relatively flat radial distribution, part of the excess population of faint  $J$ - and  $K$ -selected galaxies in the Q1126+101 field is probably unrelated to the quasar. This is consistent with the  $J-K$  and  $r-K$  color distributions, which show an excess of blue galaxies as well as of the red galaxies we expect to find at the quasar redshifts. Another possibility is a structure at the quasar redshift of size  $\geq 6 h_{75}^{-1}$  Mpc (see Sánchez & González-Serrano 1999), which is less probable but cannot be ruled out without spectroscopy or data on even wider fields.

As a measure of the richness of the structure around Q0835+580, we computed  $N_{0.5}$  (Hill & Lilly 1991), the excess number of galaxies within 0.5 Mpc of the quasar and no more than 3 mag fainter than a brightest cluster galaxy at the quasar redshift.  $N_{0.5}$  was computed as in HG98 except that galaxies  $> 140''$  from the quasar were used as the background, rather than the average literature counts. We find  $N_{0.5} = 27 \pm 11$  (corresponding to Abell richness  $2 \pm 1$ ) compared with the value of  $16 \pm 13$  found in HG98. This newer, more robust measurement illustrates the value of wide-field data in determining the background counts locally, rather than taking them from the literature or from small radii which may still be inside the large-scale structure being studied. In the case of Q1126+101, even though the overall counts in the field are higher than the literature average, wide-field data suggest that the quasar is only embedded in a small-scale overdensity.

### 3. SURFACE DENSITY OF EROS IN $1 < z < 2$ RLQ FIELDS

Since the appearance of infrared array detectors, numerous discoveries of extremely red objects (EROs) have been noted in the literature (for recent summaries see Dey et al. 1999; Daddi et al. 2000). EROs remain a poorly understood population of galaxies about which several different interpretations are plausible. Their observed colors of  $R-K \geq 6$  are so red that they seem to be explainable only by old stellar populations at  $z \gtrsim 1$  or by heavily dust-reddened galaxies or AGNs preferentially located at  $z \gtrsim 1$ . This is confirmed by the handful of spectroscopic redshifts for EROs (Dey et al. 1999; Soifer et al. 1999; Liu et al. 2000) and very red objects (VROs) as defined in § 7.3 (Cohen et al. 1999).

Previous narrow-field optical and near-IR surveys have hinted that EROs are more common along lines of sight to distant AGN (for recent summaries see Smal et al. 1999; Cimatti et al. 2000). Our  $1 < z < 2$  RLQ fields can be used to test this hypothesis more carefully, using recent estimates of the surface density of field EROs from wide-field surveys.

#### 3.1. $r-K$ -selected EROs

Thompson et al. (1999b) find 29  $K' \leq 19$  EROs with  $R-K' \geq 6$  in four fields of  $\sim 150$  arcmin<sup>2</sup> each, for a surface

density of  $0.048_{-0.009}^{+0.011}$  arcmin<sup>-2</sup> (we use the methods of Gehrels (1986) to find all  $1 \sigma$  Poissonian uncertainties where small number statistics apply). The details for one field have been published in Thompson et al. (1999a, hereafter T99). The T99  $K'$  observations were calibrated using UKIRT standards (Casali & Hawarden 1992), as were the  $K_s$  observations of HG98. We refer to both magnitudes simply as  $K$  hereafter. We also adopt  $R-K \geq 6$  as the definition of a ERO, or  $r-K \geq 6.322$  for Gunn  $r$  imaging such as ours (HG98, Appendix A), and  $K = 19$  as the division between bright and faint EROs. However, we conservatively adopt a  $3 \sigma$  detection limit in the optical instead of  $2 \sigma$  as in T99. This yields a difference of  $\sim 0.44$  mag in the lower limit on the  $r-K$  color of undetected objects.

We select EROs from all 22 RLQ fields of HGC98 with  $3 \sigma$  limits of  $r \geq 25.322$  and  $5 \sigma$  limits of  $K \geq 19$  and from the new larger area around Q1126+101 imaged with TIFKAM (§ 2.2). The total area is 160.95 arcmin<sup>2</sup>, almost identical to that of T99, and the depth of our imaging is also similar. We find 24 EROs, including two presumed stars unresolved in archival *HST* WFPC2 snapshots and one presumed star identified via its blue  $J-K$  color. Four of the remaining 21 EROs are compact enough that they could be stars given the seeing, but the rest are extended. T99 found two of their eight bright EROs to be unresolved in  $1''.1$  seeing, and both were subsequently confirmed to be stars. There is no reason to expect more stellar contamination in our ERO sample than in the T99 sample, since both are from high Galactic latitude fields of almost exactly the same total areas. Therefore we assume that only three of our 24 EROs are stars. The remaining 21  $r-K$ -selected extragalactic EROs yield a surface density of  $0.130_{-0.029}^{+0.035}$  arcmin<sup>-2</sup> to  $K = 19$ , which is 2.7 times higher than the field ERO counts of Thompson et al. (1999b) and a  $2.64 \sigma$  excess over the number expected in this area based on those counts.

This is consistent with the excesses found by the smaller surveys of Chapman, McCarthy, & Persson (2000) at  $K < 20$  around four radio galaxies with  $z \sim 1$  and Cimatti et al. (2000) at  $K \lesssim 19$  in 40 arcmin<sup>2</sup> around 14 radio-loud AGNs with  $z > 1.5$ .

#### 3.2. $J-K$ -selected EROs

Drory et al. (1999) find a surface density of  $0.098 \pm 0.009$  arcmin<sup>-2</sup> for  $K \leq 19.5$  EROs with  $J-K \geq 2.5$  from 124 objects over 1260 arcmin<sup>2</sup> from the random-field MUNICS survey (Mendes de Oliveira et al. 1998). Stellar contamination of these  $J-K$ -selected EROs should be negligible. A literature search revealed no predicted colors of  $J-K > 2.2$  for unreddened stars of any type from brown dwarf to supergiant and very few observations of objects with  $J-K > 2.5$  that were not galaxies: two objects presumed to be stars since they were unresolved on *HST* WFPC2 images (De Propriis et al. 1999) and a small number of known AGN (Cutri et al. 2000; Barkhouse & Hall 2001). Thus objects with  $J-K > 2.5$  are almost certainly not stars, are unlikely to be AGNs, and are probably galaxies.

In four RLQ fields from HGC98 with deep  $J$  data (Q0835+580, Q0952+179, Q1126+101, and Q1258+404), we find six such  $J-K$ -selected EROs. We also find three  $J-K$ -selected EROs in the new area around Q0835+580 imaged with PISCES, but none in the new area around Q1126+101 imaged with TIFKAM. Five of the EROs are from the Q1126+101 field, which as dis-

cussed in HG98 has a considerable excess of these  $J$ -band dropouts.<sup>15</sup>

Excluding the Q1126+101 field because of its excess number of these objects, we find four  $J-K$ -selected EROs in 70.373 arcmin<sup>2</sup> for a surface density of  $0.057^{+0.045}_{-0.024}$  arcmin<sup>-2</sup>, within 1  $\sigma$  of the field measurement of Drory et al. (1999). In the Q1126+101 field we find three EROs in 15.549 arcmin<sup>2</sup>, for a surface density of  $0.19^{+0.19}_{-0.09}$  arcmin<sup>-2</sup>, 3.3 times higher than in random fields, but only significant at 1.54  $\sigma$  owing to small number statistics.

We also consider the surface density of  $J$ -band dropouts in the Q1126+101 field to  $K = 20$ , since all our data reach deep enough to select EROs with  $J-K > 2.5$  to at least this magnitude. In the new TIFKAM Q1126+101 data we find six such EROs ( $0.50^{+0.30}_{-0.20}$  arcmin<sup>-2</sup>). In the HGC98 Q1126+101 data we find eight such EROs ( $0.93^{+0.46}_{-0.32}$  arcmin<sup>-2</sup>). In the other three fields with deep  $J$  data from HGC98 plus the PISCES Q0835+580 data we find 11 such EROs ( $0.16^{+0.06}_{-0.05}$  arcmin<sup>-2</sup>). The enhancement in the Q1126+101 field is still a factor of 3 or more, but remains only  $\sim 2$   $\sigma$  significance owing to small number statistics. The same holds true down to  $K = 20.5$  in the HGC98 data alone. Deeper or wider field data are unlikely to dramatically increase the statistical significance of the overdensity of  $J$ -band dropouts, but their clustered distribution within the Q1126+101 field (Fig. 24 of HG98) and the overdensity of galaxies with less extreme colors suggests that this is a physical concentration and not just a random fluctuation. However, some recent work suggests that such random field-to-field fluctuations can be quite substantial even to  $K = 20$  and beyond (see Daddi et al. 2000; Eisenhardt et al. 2000; Scodreggio & Silva 2000).

### 3.3. Extremely Red Objects: Discussion

We find bright  $r-K$ -selected EROs with  $K \leq 19$  to be 2.7 times more common in the fields of 22 RLQs with  $1 < z_q < 2$  than in the general field. We find  $J-K$ -selected EROs with  $K \leq 19.5$  to be from 1 to 3.3 times as common in the fields of four RLQs with  $1.5 < z_q < 1.75$ , depending on whether the Q1126+101 field is included or not. These quantitative measurements show that the excess ERO surface density around distant AGN is considerably smaller than previous estimates of a factor of 10 to 100 excess (Dey, Spinrad, & Dickinson 1995).

One outstanding question regarding EROs is their intrinsic luminosities. The presence of the quasars in these fields enables us to estimate the luminosities of the  $r-K$ -selected EROs by assuming that the EROs are at the quasar redshifts. This is a reasonable assumption since there is no evidence for strong or weak gravitational lensing in these fields and since the excess galaxy population is concentrated around the quasars but not correlated with the presence of intervening Mg II absorption systems (see §§ 2 and 4.3 of HG98 for details and discussion, and § 7.3 in this paper for further evidence of association).

<sup>15</sup> Two of these EROs in the Q1126+101 field have inconsistent measurements (at  $\geq 3$   $\sigma$ ) between the old HGC98 and new TIFKAM data sets. Examination of the images suggests that their  $J$  fluxes were probably underestimated in HGC98. The HGC98 KPNO 4 m IRIM data required “destriping” to remove the large-scale scattered light pattern present in some fields (see § 3.2.7 of HG98). The new  $J$  data show that this procedure worked quite well overall, but in a few cases the masking of objects was insufficient to prevent removal of some real flux.

Assuming the EROs in each field are at the redshift of the quasar in that field ( $\langle z_q \rangle = 1.61$ ) and applying elliptical  $k$ -corrections only from Fioc & Rocca-Volmerange (1997), we find  $M_K^{\text{ERO}} = -25.4 \pm 0.5$  for the  $r-K$ -selected EROs in our standard cosmology. Applying evolutionary corrections ( $e$ -corrections) from Poggianti (1997) as well, we find  $M_K^{\text{ERO}} = -24.1 \pm 0.4$ . This is consistent with the Gardner et al. (1997) measurement of  $M_K^* = -24.2 \pm 0.2$  for field galaxies at  $\langle z \rangle = 0.14\%$  ( $q_0 = 0.1$ ,  $H_0 = 75$ , and our aperture sizes (see HG98, § 5.1) and with the De Propris et al. (1998) measurement of  $M_K^* = -23.9$  in the Coma cluster.

Thus, these EROs have absolute magnitudes consistent with those expected for passively evolving luminous elliptical galaxies at the quasar redshifts, and need not be an extraordinarily luminous galaxy population. The higher density of EROs in RLQ fields can be easily understood if the RLQs are located in overdense regions. Our measured ERO luminosities are consistent with the estimated luminosity evolution in  $M_K^*$  for excess galaxies to  $K \geq 20$  in these fields (§ 5 of HG98; see also Kajisawa et al. 2000b). The faint end of our ERO distribution is set by our  $K \leq 19$  selection criterion, however, so we can say nothing further about the ERO luminosity function.

Using  $k$ - and  $e$ -corrections for bluer galaxies of later spectral types yields higher estimated luminosities for the EROs, but the red colors of these EROs strongly suggest that such corrections are not appropriate. On the other hand, if dust reddening is important for these EROs at  $z > 1$  but not for their descendants at  $z = 0$ , strong  $k$ - and  $e$ -corrections would be required. If dust were important we might expect considerable overlap between  $r-K$  and  $J-K$ -selected EROs. Thompson et al. (1999b) find that only four of 29  $r-K$ -selected EROs are  $J-K$ -selected EROs, and of our four objects with  $r-K > 6.322$  and  $J$  data, only one has  $J-K > 2.5$ . Our SED fitting (§ 7.3) yields a best-fit  $E(B-V) = 0.75 \pm 0.50$  for this object,  $E(B-V) = 0.45 \pm 0.20$  for one of the  $J-K < 2.5$  objects, and  $E(B-V) = 0$  for the remaining two  $J-K < 2.5$  objects. If the same fractions hold among the  $r-K$ -selected EROs of Thompson et al. (1999b), up to  $\sim 12$  of 29 ( $\sim 40\%$ ) could have strong dust reddening. Multicolor data on larger  $r-K$ -selected ERO samples reaching fainter magnitudes will be needed to determine how frequent and strong dust reddening really is among EROs, but for now we make no correction for dust reddening.

## 4. NARROWBAND H $\alpha$ IMAGING

H $\alpha$  is a good tracer of the instantaneous star formation rate (SFR) in galaxies (Kennicutt 1998). Narrowband surveys until recently yielded only limits on the space density of H $\alpha$  emitters at  $z > 1$ , even in the fields of quasars and radio galaxies (Pahre & Djorgovski 1995). However, in the past few years detections have been made of objects located in random fields and objects associated with damped Ly $\alpha$  absorbers, with strong intervening metal-line absorbers, or with quasars or radio galaxies (for a recent overview see Teplitz, McLean, & Malkan 1999). Given the excess galaxy population seen in our RLQ fields, they make promising targets for narrowband observations to search for H $\alpha$  emission at the quasar redshifts. In particular, we would hope to detect galaxies whose SEDs suggest they are dust-reddened and thus possibly actively star-forming and we would expect not to detect galaxies whose SEDs suggest they are old and dust-free.

The fields of Q0835+580 and Q2345+061 were imaged in  $H$  at  $0''.300 \text{ pixel}^{-1}$  and in a narrowband within  $H$  at  $0''.148 \text{ pixel}^{-1}$  using NSFCAM (Leggett & Deanult 1996)<sup>16</sup> at the NASA Infrared Telescope Facility (IRTF). Relevant details of the observations are given in Table 1. Narrowband imaging utilized a circularly variable filter (CVF) with resolution  $R = 90$  tuned to the wavelength of  $H\alpha$  at the quasar redshifts. Photometric calibration was done using UKIRT standards (Casali & Hawarden 1992). Dome flats were used in  $H$  but not for CVF imaging since the fringing across the array in CVF mode was different between dome flats and the sky. Photometry was performed in matched  $4''.2$  (14 pixel) diameter apertures on the  $H$  images and on  $H\alpha$  images resampled to the  $H$ -band pixel scale. Additional  $H$ - and narrowband observations of the fields of Q2345+061 and Q2149+212 were obtained by C. J. P. & F. D. A. H. (Table 1). These data were taken with CFHT and REDEYE ( $0''.5 \text{ pixel}^{-1}$ ) and a custom-made narrowband filter  $62 \text{ \AA}$  wide centered at  $1.6662 \mu\text{m}$ . The data were calibrated using bright objects in common with the IRTF

Q2345+061 data, and magnitudes were measured in  $4''.0$  (8 pixel) diameter apertures. To quantify the significance of the excess narrowband flux we follow Bunker et al. (1995) and use  $\Sigma$ , the number of standard deviations between the observed broadband counts and the number expected based on the narrowband counts.

There is one  $> 3 \sigma$  detection in each field observed with IRTF (see Table 2). Figure 2a shows the color-magnitude diagram for the Q0835+580 field. The  $H\alpha$  emitter—hereafter Q0835+580 ( $H\alpha 1$ )—is an unremarkable faint blue galaxy with  $\text{SFR}_{H\alpha} = 14.7 \pm 2.5 h_{75}^{-2} M_{\odot} \text{ yr}^{-1}$  using the Kennicutt (1983) relation between  $\text{SFR}_{H\alpha}$  and  $L(H\alpha)$ , which has an additional intrinsic dispersion of  $\pm 50\%$ , and assuming the detection is indeed  $H\alpha$  at the quasar redshift. With this assumption, we can also estimate  $\text{SFR}_{FUV}$  following Steidel et al. (1996) using  $U$ -band data, which have been obtained for this field (see § 7), since  $U$  samples rest-frame  $1500 \text{ \AA}$  at the quasar redshift almost exactly. Q0835+580 ( $H\alpha 1$ ) has  $U = 23.052 \pm 0.075$ , which corresponds to  $\text{SFR}_{FUV} = 5.3 \pm 0.3 h_{75}^{-2} M_{\odot} \text{ yr}^{-1}$  for a Salpeter IMF with an upper mass cutoff of  $80 M_{\odot}$ . The agreement with  $\text{SFR}_{H\alpha}$  is good given the various uncertainties (e.g., no correction for dust has been made to  $\text{SFR}_{FUV}$ ). Note that none of the

<sup>16</sup> Available at <http://irtf.ifa.hawaii.edu/online/IRTF/NFSCAM/Docs>.

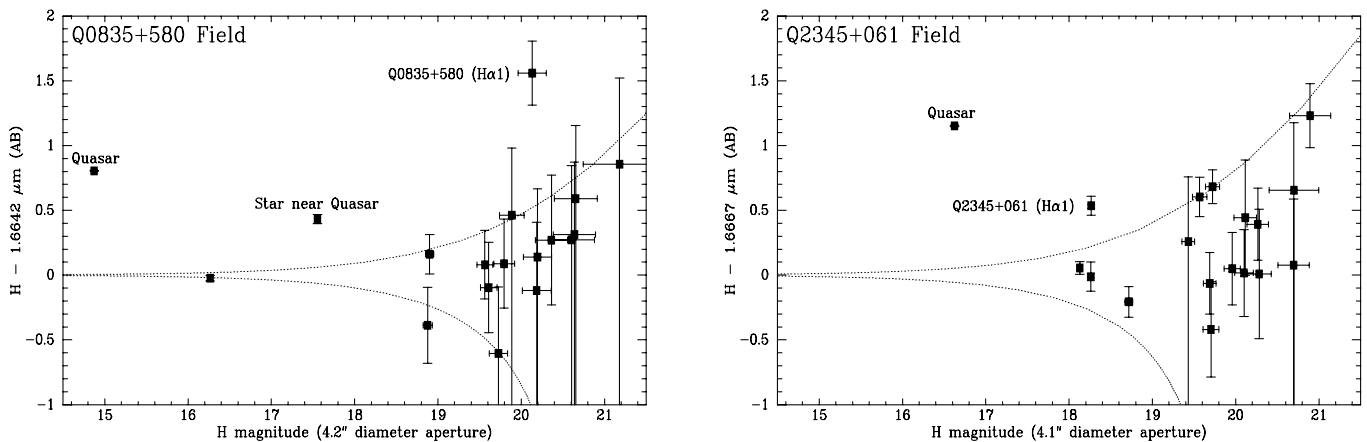


FIG. 2.—Color-magnitude diagrams from IRTF  $H$ - and narrowband imaging. Dotted lines enclose the expected range of objects with narrowband excesses of  $< 3 \sigma$  significance. *Left*: Q0835+580 field. *Right*: Q2345+061 field.

TABLE 2  
CANDIDATE  $H\alpha$  EMITTERS

ID	$H$	$(H-H\alpha)_{AB}$	$H\alpha$ REW <sup>a</sup>	$f_{H\alpha}$ <sup>b</sup>	SFR <sup>c</sup>	$z_{H\alpha}$ <sup>d</sup>	ID No. <sup>e</sup>	$\Delta\alpha$	$\Delta\delta$
Q0835+580 ( $H\alpha 1$ ).....	$20.13 \pm 0.17$	$1.56 \pm 0.25$	$316 \pm 79$	$13.9 \pm 1.3$	$14.7 \pm 1.4$	$1.5358 \pm 0.0141$	398	4.12	22.31
Q2149+212 ( $H\alpha 1$ ).....	$20.21 \pm 0.18$	$1.17 \pm 0.25$	$50.2 \pm 18.9$	$1.5 \pm 0.2$	$1.6 \pm 0.2$	$1.5389 \pm 0.0047$	171	12.48	-21.66
Q2345+061 ( $H\alpha 1$ ).....	$18.27 \pm 0.01$	$0.54 \pm 0.07$	$51.6 \pm 3.8$	$4.6 \pm 0.2$	$4.9 \pm 0.2$	$1.5396 \pm 0.0141$ <sup>f</sup>	195	-13.86	28.06
Q2345+061 ( $H\alpha 2$ ).....	$> 20.63$ ( $2 \sigma$ )	$1.78_{-0.53}^{+\infty}$	$114_{-45}^{+\infty}$	$1.7_{-0.4}^{+0.6}$	$1.8 \pm 0.5$	$1.5389 \pm 0.0047$	133	8.96	-1.08
Q2345+061 ( $H\alpha 3$ ).....	$> 20.63$ ( $2 \sigma$ )	$1.81_{-0.52}^{+\infty}$	$118_{-44}^{+\infty}$	$1.8_{-0.4}^{+0.7}$	$1.9_{-0.4}^{+0.7}$	$1.5389 \pm 0.0047$	...	22.79	21.47

NOTE.— $\Delta\alpha$  and  $\Delta\delta$  are offsets in arcseconds from the quasar in that field, with positive offsets to the north and east.

<sup>a</sup> Rest equivalent width in angstroms, calculated from eq. (5) of Bunker et al. 1995.

<sup>b</sup> Units of  $10^{-17} \text{ ergs cm}^{-2} \text{ s}^{-1}$ , calculated from eq. (6) of Bunker et al. 1995 using the appropriate zero point.

<sup>c</sup> Star formation rate in units of  $M_{\odot} \text{ yr}^{-1}$  for  $H_0 = 75 \text{ km s}^{-1} \text{ Mpc}^{-1}$ ,  $q_0 = 0.1$ , derived from the relation of Kennicutt 1983.

<sup>d</sup> Possible redshift range determined from the bandpass of the filter in which the excess was detected.

<sup>e</sup> Identification number in our catalog of the field (available on request from the first author; see Table 4.)

<sup>f</sup> Excluding the range  $1.5389 \pm 0.0047$  (see text).

dozen or so galaxies with  $r - K \gtrsim 5$  immediately surrounding Q0835+580 were detected in  $H\alpha$ . If they are at the quasar redshift, they must have star formation rates of  $< 1.8 h_{75}^{-2} M_{\odot} \text{ yr}^{-1}$  ( $3 \sigma$ ), consistent with them being red because of age and/or metallicity rather than being extremely dust-reddened starburst galaxies (see § 7).

Figure 2b shows the IRTF data color-magnitude diagram of the Q2345+061 field, and Figure 3a the same diagram for the CFHT data. Figure 4a shows the  $H\alpha$  image with the  $H\alpha$  emitters marked. The candidate  $H\alpha$  emitter seen with IRTF—Q2345+061 ( $H\alpha 1$ )—is not confirmed with CFHT,

but the CFHT narrowband filter is much narrower than the IRTF CVF and the line could lie outside the wavelength range of the CFHT filter. There are also two objects visible in the narrowband CFHT image but not on the  $H$ -band CFHT image. They both have  $H\alpha$  excesses of  $3 \sigma$  significance with  $H - H\alpha \gtrsim 1.7$  (Fig. 3a and Table 2). Q2345+061 ( $H\alpha 2$ ) is detected at  $H = 20.3 \pm 0.1$  and  $H - H\alpha = 0.4 \pm 0.3$  in the IRTF data while Q2345+061 ( $H\alpha 3$ ) is not detected in the IRTF  $H\alpha$  image or in the deep  $K_s$  data of HGC98 to  $K_s > 21.7$ . It may be detected at  $H \sim 21.5 \pm 0.5$  in the IRTF data and at  $r \sim 25.1 \pm 0.5$  in the  $r$  data of HGC98. In

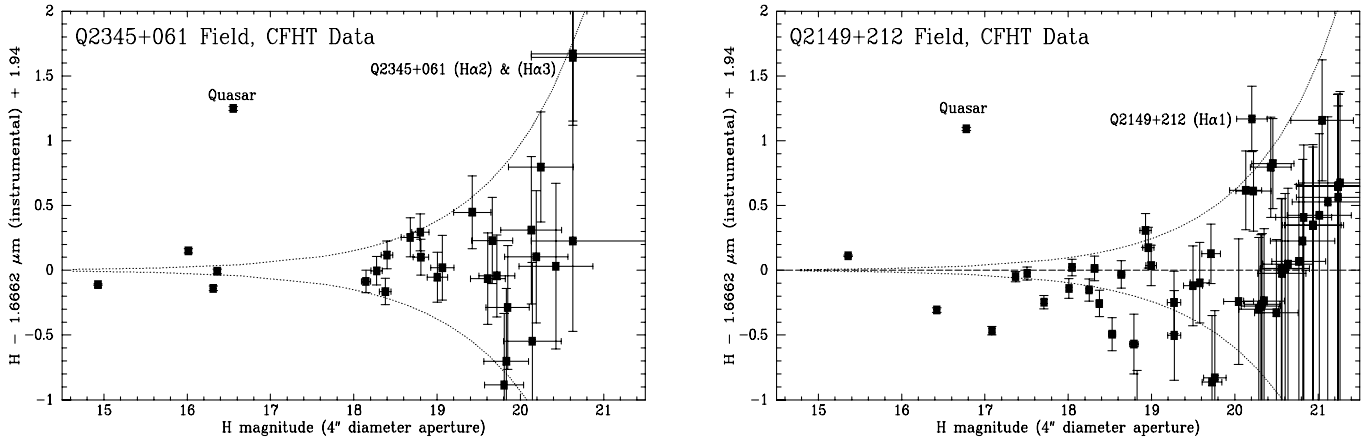


FIG. 3.—Color-magnitude diagrams from CFHT  $H$ - and narrowband imaging. Dotted lines enclose the expected range of objects with narrowband excesses of  $< 3 \sigma$  significance. *Left*: Q2345+061 field. The two candidate  $3 \sigma$   $H\alpha$  emitters have  $H \geq 20.6$  and  $H - H\alpha \gtrsim 1.7$ . The three bright objects outside the  $3 \sigma$  significance range range are galaxies larger than the  $2''.0$  radius photometric aperture. *Right*: Q2149+212 field. The candidate  $H\alpha$  emitter has  $H \sim 20.2$  and  $H - H\alpha \sim 1.2$ .

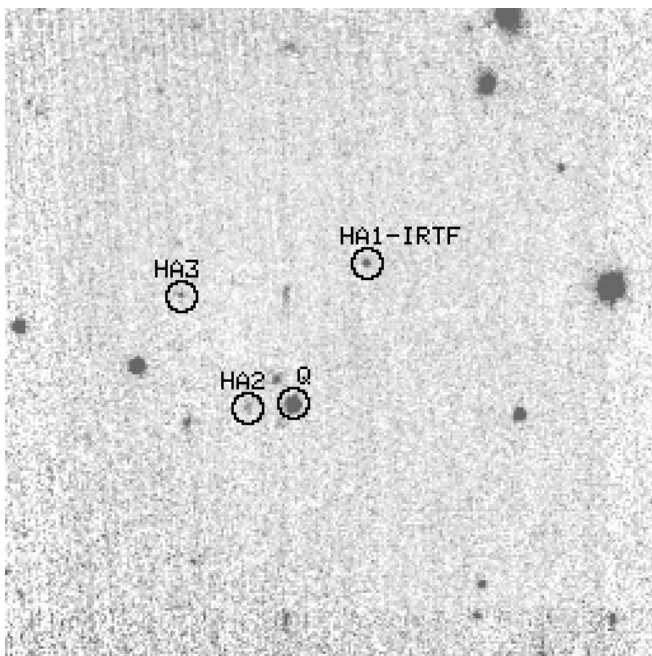


FIG. 4a

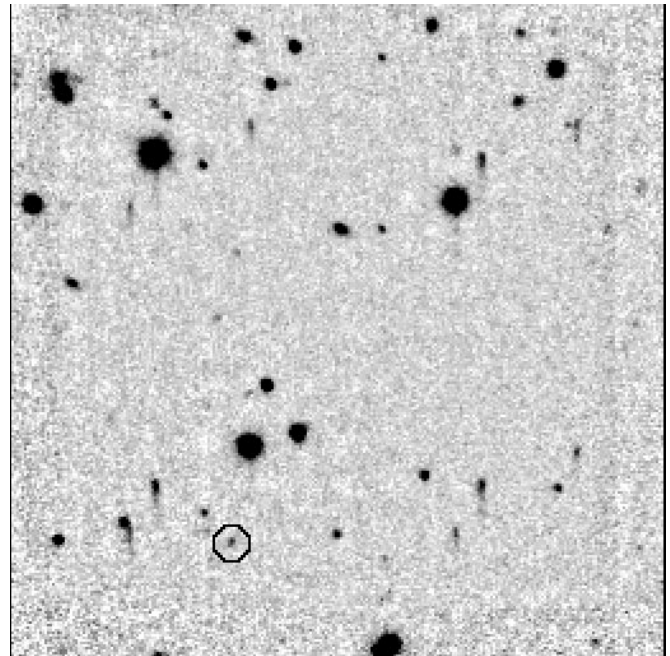


FIG. 4b

FIG. 4.—CFHT REDEYE narrowband  $H\alpha$  images, each  $128'' \times 128''$ . North is up, and east is to the left. Bright objects produce elongated crosstalk “images” at the same position in the other three quadrants. (a) Q2345+061 field. The candidate  $H\alpha$  emitters are marked, including one selected as a candidate only in IRTF data. (b) Q2149+212 field. The quasar is the brightest object in the southeast quadrant. The candidate  $H\alpha$  emitter is marked.

any case, given the photometric uncertainties, the CFHT and IRTF  $H\alpha$  measurements are consistent for both Q2345+061 ( $H\alpha 2$ ) and Q2345+061 ( $H\alpha 3$ ).

Figure 3b shows the color-magnitude diagram for the CFHT data on the Q2149+212 field. There is one candidate  $H\alpha$  emitter, with  $H \sim 20.2$  (Fig. 4b and Table 2). It is a fairly red galaxy with  $r-K = 5$  and  $H-K \sim 1$ . This object is confirmed as an  $H\alpha$  emitter in additional data taken the same night but not used because of calibration problems, whereas the object at  $H \sim 19$  and  $H-H\alpha \sim 0.3$  is not confirmed.

Our  $H\alpha$  imaging reaches flux limits of  $1$  to  $2 \times 10^{-17}$  ergs  $\text{cm}^{-2} \text{s}^{-1}$  ( $3 \sigma$ ), deeper than any previously published survey due to the very long IRTF CVF exposures and the very low background in the CFHT narrowband images. Five detections in  $10.156 \text{ arcmin}^2$  (counting both observations of the Q2345+061 field since different filters were used) gives a surface density of  $0.5^{+0.3}_{-0.2} \text{ arcmin}^{-2}$ . For comparison, no  $H\alpha$  sources were found in two random fields surveyed to  $0.8 \times 10^{-17}$  ergs  $\text{cm}^{-2} \text{s}^{-1}$  ( $3 \sigma$ ) with the same CFHT setup as in this work, for a  $1 \sigma$  upper limit of  $0.2$  sources per  $\text{arcmin}^2$  (Pritchett & Hartwick 2001).

In the deepest published survey, McCarthy et al. (1999) find  $0.57$  sources per  $\text{arcmin}^2$  to  $4.1 \times 10^{-17}$  ergs  $\text{cm}^{-2} \text{s}^{-1}$  ( $3 \sigma$ ) from slitless spectroscopy of random fields with NICMOS. We find only  $0.2$  sources per square arcminute to the same limit, but they sample a redshift range of  $\Delta z = 1.2$  compared with our average  $\Delta z = 0.013$ . Our surface density is approximately  $32$  times higher, although that number is biased high because we targeted a redshift where we had reason to believe a galaxy excess existed. In surveys at the redshifts of quasars and radio galaxies, Pahre & Djorgovski (1995), van der Werf (1997) and Teplitz, McLean, & Malkan (1999) found four sources in  $242 \text{ arcmin}^2$  to limits of  $9$  to  $19 \times 10^{-17}$  ergs  $\text{cm}^{-2} \text{s}^{-1}$  ( $3 \sigma$ ). We find at most one source in  $10.156 \text{ arcmin}^2$  to these depths, which is consistent with the previous surveys due to small number statistics even though it is formally up to a factor of six excess.

In summary, our fields represent a factor of  $2.5$  excess compared with the only existing random-field survey to equal depth, a factor of  $\leq 32$  excess compared with the deepest published random-field survey, and a factor of  $\leq 6$  excess compared with previous AGN-field surveys.

The fields studied in this paper are among the best candidates for  $1 < z < 2$  RLQs in clusters from a survey of 31 (Hall, Green, & Cohen 1998), so this excess is not unexpected. These  $H\alpha$  detections constitute more evidence that the galaxy overdensities in these RLQ fields are real, and

that at least some of the excess galaxies are at the quasar redshifts. Although the number of member galaxies in the candidate host clusters of Q2149+212 and Q2345+061 is unknown, the deep CFHT  $H\alpha$  images show that there are only three such galaxies with star formation rates of  $\gtrsim 1.5 h_{75}^{-1} M_{\odot} \text{ yr}^{-1}$  within fields  $0.95 h_{75}^{-1} \text{ Mpc}$  wide centered on these quasars. This is a lower limit which neglects extinction and the velocity dispersion of the clusters (e.g., Q2345+061 ( $H\alpha 1$ ) is not detected in the narrow CFHT filter), but it is still a stringent limit which illustrates the potential of deep wide-field narrowband data in studying star formation rates in high-redshift clusters.

## 5. SUBMILLIMETER MAPPING

In the last few years it has become clear that much of the star formation activity in the universe is obscured by dust and can be easily detected only at far-IR and submillimeter wavelengths (e.g., Dwek et al. 1998; Smail et al. 1998). The presence of a number of galaxies with SEDs strongly indicative of substantial dust reddening in our RLQ fields suggested that they might be detectable submillimeter sources. Thus we obtained continuum observations at  $450$  and  $850 \mu\text{m}$  with SCUBA (the Submillimeter Common-User Bolometer Array, Holland et al. 1998), on the James Clerk Maxwell Telescope. Details of the observations are given in Table 1. All observations used standard 64-point jiggle maps to fully sample both arrays.

Data on Q2345+061 were obtained (and reduced) as a service observing program. Azimuthal chopping and nodding was used. No sources are seen at  $450 \mu\text{m}$ , but at  $850 \mu\text{m}$  Q2345+061 is detected at  $2.8 \sigma$  (Table 3). No other potential sources (e.g., the  $H\alpha$  emitters) are seen, but we are only sensitive to hyperluminous IR galaxies ( $L_{\text{FIR}} > 10^{13} h_{50}^{-2} L_{\odot}$ ). The  $2 \sigma$  limit at  $850 \mu\text{m}$  corresponds to  $\sim 1.3 \times 10^{13} h_{50}^{-2} L_{\odot}$  for the quasar redshift and a bolometric correction calculated using a dust emissivity spectral index of  $1.0$  and the Arp 220 dust temperature  $T = 47 \text{ K}$ , following Barger et al. (1999).

Observations of Q0835+580 and Q1126+101 were made using a fixed chop throw of  $40''$  and  $12''36$  offsets north or south every other measurement. Conditions ranged from fair to excellent during the run. The data were reduced and calibrated in the standard manner using SURF (Jenness & Lightfoot 1998). Figures 5 and 6 show  $850 \mu\text{m}$  contours superposed on  $K$  images of the Q0835+580 and Q1126+101 fields, respectively. The  $450 \mu\text{m}$  maps are not shown as no objects were detected at that wavelength in either field. To help reject spurious sources, we cross-

TABLE 3  
PROBABLE AND POSSIBLE SUBMILLIMETER DETECTIONS

Source	$\Delta\alpha$	$\Delta\delta$	S/N	$S_{850}$ (mJy)	CC	Catalog ID	Notes
Q2345+061 .....	0	0	2.8	11.7	...	157	...
Q0835+580 (SM1).....	8.5	-44.8	4.6	10.1	0.37	117	Tentative
Q0835+580 (SM2).....	14.7	36.1	3.4	7.5	0.29	458	Tentative
Q1126+101 .....	-2.0	-0.7	3.4	6.2	0.49	350	...
Q1126+101 (SM1).....	-14.7	14.7	3.0	5.5	0.46	384	...
Q1126+101 (SM2).....	-45.7	-13.7	4.4	8.0	0.71	...	...
Q1126+101 (SM3).....	-47.4	-70.6	6.7	12.6	0.69	...	Tentative; edge

NOTES.— $\Delta\alpha$  and  $\Delta\delta$  are offsets in arcseconds relative to the optical position of the quasar. CC is the correlation coefficient for each source. Catalog ID is the identification number of the possible optical/near-IR counterpart(s) in our catalogs of these fields (available on request from the first author; see Table 4).

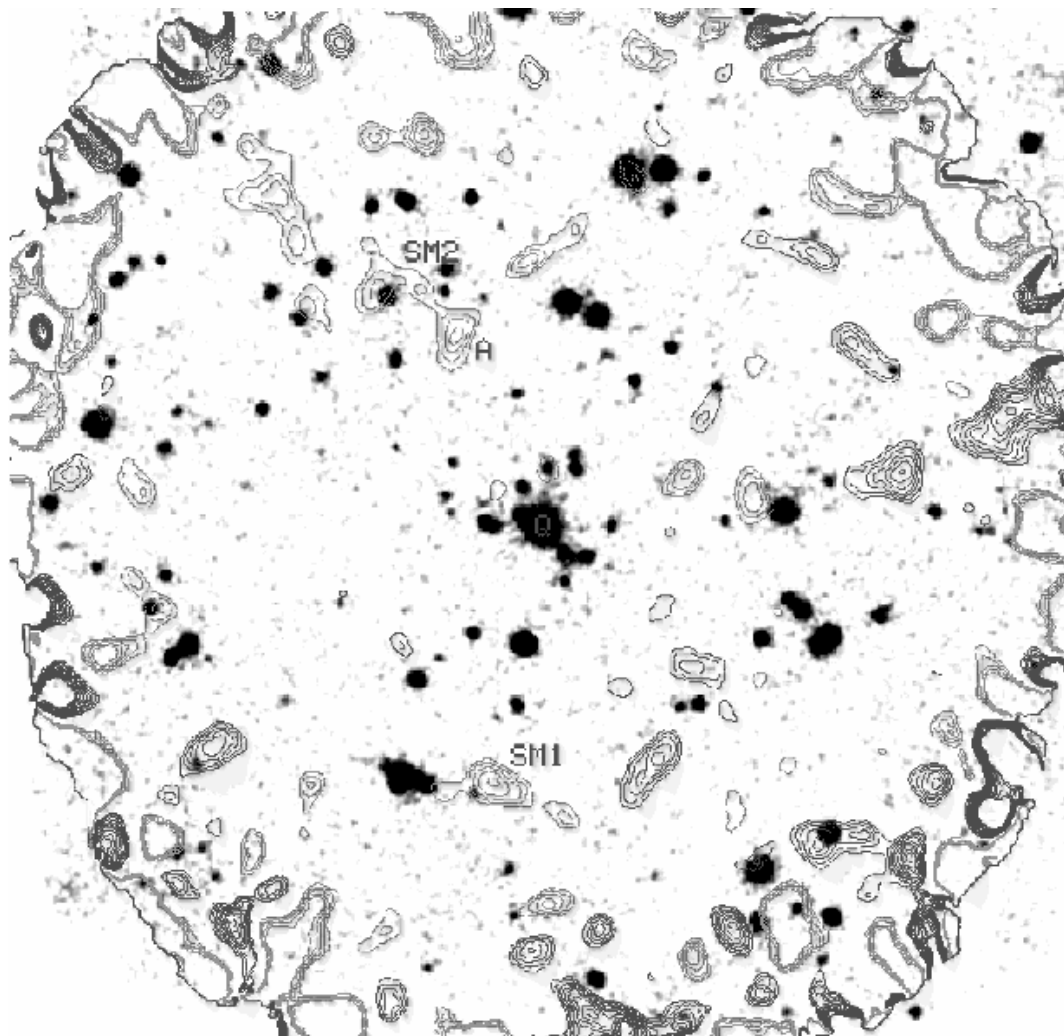


FIG. 5.— $K$  image of the Q0835+580 field (data from HGC98) overlaid with 850  $\mu\text{m}$  SCUBA contours (this paper, 7.04 ks exposure,  $1\sigma$  rms noise  $2.21\text{ mJy beam}^{-1}$ ). The submillimeter and optical images have been aligned using the default JCMT pointing. Light contours are positive ( $2.5, 3.0, 3.5, \dots\sigma$ ) and dark contours are negative ( $-2.5, -3.0, -3.5, \dots\sigma$ ), with the outermost dark contour marking the edge of the full SCUBA maps. The quasar is marked by “Q,” and submillimeter sources are discussed in the text by SM number. Positive features marked by a letter (or not marked at all) do not correspond to peaks in the cross-correlation map and so are not considered real. [See the electronic edition of the *Journal* for a color version of this figure.]

correlated the maps with the beam as given by a calibration observation of an unresolved source on the same night. Each pixel’s value in the cross-correlation map measures how closely the submillimeter map centered on that pixel resembles the beam, providing a measure of the correlation coefficient (CC) for each tentative source. Real high-redshift objects should resemble the beam quite closely, since objects more extended than a point source cannot be at high redshift given the large JCMT beam, and objects more compact than a point source might be just noise.

There are two  $\geq 3.5\sigma$  sources in the Q0835+580 field, which coincide with peaks in the cross-correlation map, but the bright source (SM1; 10.1 mJy) has only CC = 0.37, and the faint source (SM2; 7.5 mJy) only CC = 0.29. There are nearly equal numbers of negative and positive peaks at these flux and CC values, so we regard both these sources as tentative submillimeter detections. However, they both have possible optical/IR identifications: a  $K = 19.8$  moderately blue galaxy (Q0835+580 (117),  $r-K = 3.9$ )  $3.2'$  from the position of SM1, and a  $K = 17.7$  red galaxy [Q0835+580 (458)],  $r-K = 5.4$ )  $2.1'$  from the position of

SM2. The identification numbers of these objects refer to our optical/NIR catalogs of these fields, available on request from the first author. We include information on these objects in Table 3 (and Table 4), but we emphasize that we do not consider them unambiguous submillimeter detections. Both objects are faint enough in the optical and near-infrared that they could be at the quasar redshift; Q0835+580 (SM2) would be 0.4 mag brighter than the magnitude of a brightest cluster galaxy (as estimated in HG98) if it was at the quasar redshift, but this is within the observed scatter in such objects’ magnitudes at  $z \simeq 1$  (Thompson, Aftreth, & Soifer 2000). We discuss these objects further in § 7.1.4. Note that Q0835+580 (Hz1) is not detected, although the  $3\sigma$  limit of  $\text{SFR}_{\text{FIR}} < 2090 \pm 550 h_{75}^{-2} M_{\odot} \text{ yr}^{-1}$  (calculated following Dey et al. 1999, using a Salpeter IMF and assuming it is at the quasar redshift) is 2 orders of magnitude larger than  $\text{SFR}_{\text{UV}}$  and  $\text{SFR}_{\text{Hz}}$  for this object (§ 4).

In the Q1126+101 field, the quasar and several other sources are present with  $\geq 3\sigma$  and CC > 0.33. There are twice as many fluctuations above sky as below sky at these

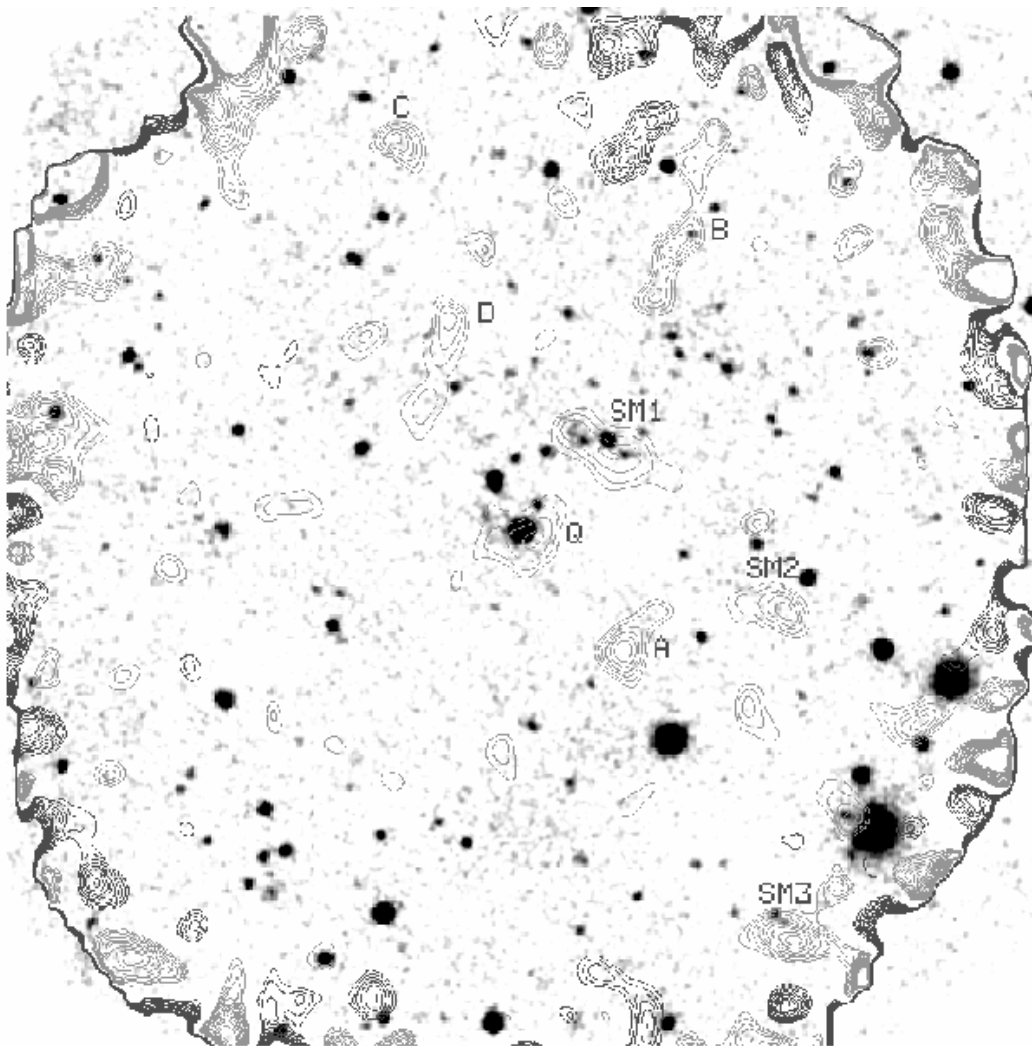


FIG. 6.— $K$  image of the Q1126+101 field (data from HGC98) overlaid with  $850\ \mu\text{m}$  SCUBA contours (this paper, 15.36 ks exposure,  $1\ \sigma$  rms noise  $1.83\ \text{mJy beam}^{-1}$ ). Feature A, although strong, was seen only on night 2 and is probably noise. See Fig. 5 for further details. [See the electronic edition of the *Journal* for a color version of this figure.]

flux and CC values in this field; thus, some of the detections are probably real but some are probably spurious. Overall the most reliable detections are the quasar and SM1. Despite their low S/N, they were clearly detected on both nights, have high correlation coefficients, and have FWHM  $\sim 14''$  as expected for the JCMT beam at  $850\ \mu\text{m}$ . The possible counterpart  $1'1''$  to the north of SM1, object Q1126+101 (384), is discussed further in § 7.2.1. The two other sources listed in Table 3 are less certain, despite their higher S/N on the raw map. They have FWHM  $\sim 9''$ , suggesting they might be noise spikes rather than actual objects. Neither Q1126+101 (SM2) nor (SM3) have probable identifications in the optical/IR data.

#### 6. CFHT ADAPTIVE-OPTICS IMAGING

Little information is available on the detailed morphologies of EROs, although our knowledge is growing rapidly (Dey et al. 1999; T99; Benítez et al. 1999; Moriondo, Cimatti, & Daddi 2000; Stiavelli & Treu 2000). To improve this situation,  $H$ -band adaptive-optics data were obtained with the CFHT adaptive optics bonnette (known as PUEO)

and the KIR camera ( $1024^2$  HgCdTe detector,  $0''.0348\ \text{pixel}^{-1}$ ). The  $V = 10.3$  star BD+58 1138 was used to guide on a field  $\sim 35''$  from the star and  $\sim 90''$  from Q0835+580. Standard infrared observing and reduction procedures were used, including dome flats for flattening. Photometry was done using UKIRT standards and assuming a typical Mauna Kea  $H$ -band extinction coefficient of  $0.051 \pm 0.012$  (Krisciunas et al. 1987). Natural seeing conditions during the observations were poor, resulting in FWHM after correction of  $\sim 0''.42$ , as measured from the most compact object on the image.

The KIR field contains two objects bright enough for image profile analysis. The fainter, redder object is designated Q0835+580 (106) since it is object 106 in our catalog of this field and has  $K_s = 17.7$ ,  $r-K = 5$  and  $J-K = 2$ . The other object, Q0835+580 (112), has  $K_s = 17.3$  and  $r-K = 2.4$ . Radial profile analysis shows that both galaxies are much better fit by an  $r^{1/4}$  law profile than by an exponential disk profile, with  $r_e = 0''.97 \pm 0''.14$  for Q0835+580 (106) and  $r_e = 0''.49 \pm 0''.07$  for Q0835+580 (112).

The resolution was not high enough for further morphological analysis, but if we assume the objects are early-type

TABLE 4

## SED-FITTING RESULTS

ID	$\Delta\alpha$	$\Delta\delta$	K	r-K	J-K	z-J	Model	$\chi^2_\nu$	$z_{\text{ph}}$	$E(B-V)$	Age	Notes
Q0835+580 Field Objects												
65.....	5.5	-58.7	19.52 ± 0.08	5.59 ± 0.21	1.92 ± 0.08	2.80 ± 0.19	Burst	1.23	1.70 <sup>+0.40</sup> <sub>-0.30</sub>	0.28 <sup>+0.62</sup> <sub>-0.60</sub>	0.36 <sup>+0.36</sup> <sub>-0.36</sub>	VRO
106.....	-37.1	-67.9	17.73 ± 0.02	5.05 ± 0.04	2.10 ± 0.03	1.81 ± 0.03	Burst	5.83	4.50 <sup>+0.15</sup> <sub>-0.15</sub>	0.23 <sup>+0.25</sup> <sub>-0.18</sub>	0.055 <sup>+0.126</sup> <sub>-0.052</sub>	AO Target
112.....	-49.6	-67.2	15.32 ± 0.02	3.64 ± 0.02	1.46 ± 0.02	1.60 ± 0.01	Const	19.60	3.10 <sup>+0.05</sup> <sub>-0.05</sub>	0.00 <sup>+0.02</sup> <sub>-0.02</sub>	0.806 <sup>+0.472</sup> <sub>-0.166</sub>	AO Target
117.....	11.4	-46.1	19.83 ± 0.13	3.91 ± 0.11	1.16 ± 0.10	2.16 ± 0.10	Burst	2.19	1.60 <sup>+0.15</sup> <sub>-0.15</sub>	0.00 <sup>+0.12</sup> <sub>-0.12</sub>	0.286 <sup>+0.125</sup> <sub>-0.125</sub>	Q0835+580 (SM1)
248.....	-8.0	-14.9	20.88 ± 0.20	5.08 ± 0.33	1.75 ± 0.17	> 2.66	Const	1.33	1.55 <sup>+0.45</sup> <sub>-0.40</sub>	0.28 <sup>+0.62</sup> <sub>-0.10</sub>	19.50 <sup>+0.50</sup> <sub>-19.49</sub>	SCG
280.....	63.8	-8.6	18.96 ± 0.07	5.48 ± 0.18	1.85 ± 0.06	3.07 ± 0.23	Burst	17.00	1.85 ± 0.20	0.46 <sup>+0.19</sup> <sub>-0.19</sub>	0.64 <sup>+0.64</sup> <sub>-0.44</sub>	VRO
307.....	-18.9	3.5	20.95 ± 0.22	4.49 ± 0.28	1.30 ± 0.19	2.24 ± 0.22	Const	11.50	1.15 <sup>+0.35</sup> <sub>-0.30</sub>	0.20 <sup>+0.22</sup> <sub>-0.22</sub>	19.50 <sup>+0.50</sup> <sub>-17.10</sub>	SCG
319.....	16.0	5.0	19.27 ± 0.07	3.30 ± 0.07	1.55 ± 0.08	1.68 ± 0.07	Burst	1.56	2.20 <sup>+0.15</sup> <sub>-0.35</sub>	0.24 <sup>+0.14</sup> <sub>-0.12</sub>	0.026 <sup>+0.054</sup> <sub>-0.019</sub>	SCG
320.....	15.3	1.9	20.23 ± 0.11	4.99 ± 0.21	1.94 ± 0.13	2.65 ± 0.29	Const	2.63	1.75 <sup>+0.50</sup> <sub>-0.40</sub>	0.30 <sup>+0.35</sup> <sub>-0.16</sub>	20.00 <sup>+0.09</sup> <sub>-0.15</sub>	SCG
329.....	-19.8	7.6	19.98 ± 0.11	3.98 ± 0.14	1.54 ± 0.13	1.81 ± 0.12	Const	1.49	1.45 <sup>+0.40</sup> <sub>-0.25</sub>	0.12 <sup>+0.16</sup> <sub>-0.10</sub>	4.75 <sup>+4.35</sup> <sub>-4.35</sub>	SCG
333.....	14.9	10.5	20.00 ± 0.11	3.96 ± 0.09	1.34 ± 0.08	2.27 ± 0.09	Burst	4.11	1.95 <sup>+0.20</sup> <sub>-0.35</sub>	0.00 <sup>+0.55</sup> <sub>-0.00</sub>	0.29 <sup>+0.11</sup> <sub>-0.29</sub>	SCG
339.....	-6.0	9.5	18.64 ± 0.04	> 7.03	1.99 ± 0.04	3.55 ± 0.20	Burst	5.57	1.65 <sup>+0.25</sup> <sub>-0.20</sub>	0.01 <sup>+0.19</sup> <sub>-0.19</sub>	19.75 <sup>+0.25</sup> <sub>-0.60</sub>	SCG, ERO
340.....	-5.7	11.8	19.91 ± 0.08	5.69 ± 0.25	1.98 ± 0.08	> 2.78	Burst	1.70	1.70 <sup>+0.20</sup> <sub>-0.20</sub>	0.42 <sup>+0.43</sup> <sub>-0.28</sub>	0.23 <sup>+0.23</sup> <sub>-0.23</sub>	SCG
343.....	-12.2	-0.1	19.06 ± 0.06	4.95 ± 0.10	1.59 ± 0.05	2.93 ± 0.12	Const	2.92	1.60 <sup>+0.25</sup> <sub>-0.25</sub>	0.32 <sup>+0.12</sup> <sub>-0.14</sub>	2.75 <sup>+17.25</sup> <sub>-2.24</sub>	SCG, red z - J
345.....	3.7	11.0	21.06 ± 0.30	2.79 ± 0.21	0.80 ± 0.22	2.05 ± 0.14	Burst	1.22	2.20 <sup>+0.30</sup> <sub>-0.30</sub>	0.00 <sup>+0.71</sup> <sub>-0.43</sub>	0.18 <sup>+0.46</sup> <sub>-0.71</sub>	SCG
347.....	-3.8	-9.9	19.53 ± 0.07	> 6.79	1.86 ± 0.06	> 3.89	Burst	7.96	1.75 <sup>+0.30</sup> <sub>-0.30</sub>	0.46 <sup>+0.19</sup> <sub>-0.19</sub>	0.72 <sup>+0.89</sup> <sub>-0.89</sub>	SCG, ERO, radio hotspot
348.....	-11.2	-7.3	20.51 ± 0.19	2.82 ± 0.13	1.25 ± 0.14	2.03 ± 0.13	Burst	2.02	2.20 <sup>+0.30</sup> <sub>-2.00</sub>	0.01 <sup>+0.37</sup> <sub>-0.01</sub>	0.09 <sup>+0.07</sup> <sub>-0.09</sub>	SCG
349.....	-1.2	9.6	19.18 ± 0.06	5.73 ± 0.18	1.69 ± 0.05	2.97 ± 0.14	Burst	2.94	1.65 <sup>+0.30</sup> <sub>-0.30</sub>	0.32 <sup>+0.18</sup> <sub>-0.18</sub>	0.29 <sup>+0.73</sup> <sub>-0.18</sub>	SCG, VRO
352.....	9.3	0.3	18.00 ± 0.02	3.25 ± 0.02	1.32 ± 0.02	1.83 ± 0.02	Burst	5.40	0.35 <sup>+0.20</sup> <sub>-0.05</sub>	0.16 <sup>+0.06</sup> <sub>-0.06</sub>	0.11 <sup>+0.05</sup> <sub>-0.10</sub>	SCG
353.....	9.7	3.2	20.85 ± 0.15	3.03 ± 0.11	1.45 ± 0.13	1.59 ± 0.10	Burst	0.02	2.30 <sup>+0.30</sup> <sub>-2.20</sub>	0.26 <sup>+0.29</sup> <sub>-0.26</sub>	0.064 <sup>+19.936</sup> <sub>-0.064</sub>	SCG
354.....	3.1	6.3	18.90 ± 0.05	3.28 ± 0.04	1.27 ± 0.04	1.67 ± 0.03	Const	0.67	1.82 <sup>+0.43</sup> <sub>-0.43</sub>	0.60 <sup>+0.98</sup> <sub>-0.60</sub>	0.001 <sup>+0.160</sup> <sub>-0.001</sub>	SCG
355.....	-7.8	-5.5	18.74 ± 0.03	5.26 ± 0.07	1.71 ± 0.03	2.74 ± 0.07	Burst	1.05	1.70 <sup>+0.15</sup> <sub>-0.15</sub>	0.34 <sup>+0.16</sup> <sub>-0.16</sub>	0.20 <sup>+0.37</sup> <sub>-0.13</sub>	SCG, VRO
356.....	-3.9	-5.1	19.37 ± 0.04	5.80 ± 0.13	1.88 ± 0.04	2.73 ± 0.09	Const	2.23	1.45 <sup>+0.25</sup> <sub>-0.20</sub>	0.32 <sup>+0.18</sup> <sub>-0.04</sub>	19.00 <sup>+1.00</sup> <sub>-17.57</sub>	red z - J
379.....	62.0	19.0	19.47 ± 0.08	4.91 ± 0.16	1.53 ± 0.07	3.02 ± 0.23	Burst	1.03	1.85 <sup>+0.25</sup> <sub>-0.25</sub>	0.12 <sup>+0.22</sup> <sub>-0.22</sub>	0.45 <sup>+0.58</sup> <sub>-0.45</sub>	Q0835+580 (Hα1)
398.....	4.1	22.3	19.20 ± 0.08	3.20 ± 0.06	1.38 ± 0.06	1.70 ± 0.05	Burst	0.32	2.20 <sup>+0.25</sup> <sub>-0.25</sub>	0.34 <sup>+0.16</sup> <sub>-0.34</sub>	0.003 <sup>+0.140</sup> <sub>-0.000</sub>	VRO
440.....	41.1	35.2	18.59 ± 0.04	5.65 ± 0.11	1.72 ± 0.04	2.27 ± 0.06	Burst	17.10	1.05 <sup>+0.25</sup> <sub>-0.10</sub>	0.34 <sup>+0.21</sup> <sub>-0.26</sub>	0.72 <sup>+0.59</sup> <sub>-0.72</sub>	Q0835+580 (SM2)
458.....	26.2	38.9	17.72 ± 0.02	5.35 ± 0.04	2.03 ± 0.02	2.24 ± 0.03	Burst	0.23	1.20 <sup>+0.10</sup> <sub>-0.10</sub>	0.55 <sup>+0.05</sup> <sub>-0.05</sub>	0.035 <sup>+0.018</sup> <sub>-0.035</sub>	VRO
461.....	45.9	39.8	18.60 ± 0.06	5.63 ± 0.15	2.01 ± 0.06	2.65 ± 0.14	Const	4.55	1.45 <sup>+0.35</sup> <sub>-0.40</sub>	0.36 <sup>+0.29</sup> <sub>-0.06</sub>	19.50 <sup>+0.50</sup> <sub>-18.99</sub>	VRO
478.....	72.0	41.7	18.27 ± 0.04	5.63 ± 0.14	2.00 ± 0.05	2.72 ± 0.12	Burst	4.27	1.65 <sup>+0.35</sup> <sub>-0.90</sub>	0.80 <sup>+0.50</sup> <sub>-0.60</sub>	0.004 <sup>+0.720</sup> <sub>-0.004</sub>	VRO
479.....	69.4	44.8	19.07 ± 0.06	5.53 ± 0.21	1.99 ± 0.07	2.36 ± 0.14	Const	2.85	1.15 <sup>+0.35</sup> <sub>-0.35</sub>	0.32 <sup>+0.08</sup> <sub>-0.08</sub>	19.25 <sup>+0.21</sup> <sub>-0.21</sub>	VRO
483.....	36.9	43.8	18.18 ± 0.04	5.88 ± 0.12	1.82 ± 0.03	2.61 ± 0.07	Burst	0.43	1.60 <sup>+0.35</sup> <sub>-0.15</sub>	0.24 <sup>+0.14</sup> <sub>-0.10</sub>	0.72 <sup>+0.46</sup> <sub>-0.46</sub>	VRO

TABLE 4—Continued

ID	$\Delta\alpha$	$\Delta\delta$	$K$	$r-K$	$J-K$	$z-J$	Model	$\chi^2_\nu$	$z_{\text{ph}}$	$E(B-V)$	Age	Notes
Q1126+101 Field Objects												
66	.....	-19.9	19.50 ± 0.13	6.09 ± 0.31	1.45 ± 0.10	3.53 ± 0.21	Burst	18.40	1.40 <sup>+0.25</sup> <sub>-0.10</sub>	0.03 <sup>+0.05</sup> <sub>-0.03</sub>	17.25 <sup>+2.75</sup> <sub>-12.75</sub>	VRO
91	.....	-10.3	19.49 ± 0.12	5.70 ± 0.24	1.84 ± 0.11	2.74 ± 0.17	Burst	2.68	5.00 <sup>+0.09</sup> <sub>-0.33</sub>	0.60 <sup>+0.15</sup> <sub>-0.36</sub>	0.005 <sup>+0.220</sup> <sub>-0.005</sub>	VRO
269	.....	-35.7	20.46 ± 0.24	4.38 ± 0.32	0.88 ± 0.25	> 3.694	Burst	9.98	1.90 <sup>+0.25</sup> <sub>-0.35</sub>	0.20 <sup>+0.20</sup> <sub>-0.20</sub>	0.72 <sup>+0.54</sup> <sub>-0.54</sub>	red $z-J$
298	.....	-28.0	19.32 ± 0.09	5.71 ± 0.22	1.73 ± 0.09	3.29 ± 0.23	Burst	0.21	1.90 <sup>+0.30</sup> <sub>-0.35</sub>	0.22 <sup>+0.48</sup> <sub>-0.22</sub>	0.45 <sup>+0.98</sup> <sub>-0.45</sub>	VRO
346	.....	1.0	19.34 ± 0.08	6.15 ± 0.24	1.69 ± 0.07	3.10 ± 0.14	Burst	6.59	1.40 <sup>+0.30</sup> <sub>-0.15</sub>	0.00 <sup>+0.12</sup> <sub>-0.00</sub>	20.00 <sup>+0.00</sup> <sub>-1.50</sub>	VRO
370	.....	49.1	18.64 ± 0.05	5.96 ± 0.16	2.31 ± 0.07	2.54 ± 0.13	Const	0.03	1.40 <sup>+0.10</sup> <sub>-1.20</sub>	0.44 <sup>+0.10</sup> <sub>-0.10</sub>	15.75 <sup>+2.75</sup> <sub>-15.75</sub>	VRO
381	.....	-10.9	19.36 ± 0.07	5.65 ± 0.17	2.69 ± 0.14	> 3.36	Const	12.10	1.95 <sup>+0.45</sup> <sub>-0.35</sub>	0.55 <sup>+0.40</sup> <sub>-0.11</sub>	17.25 <sup>+2.75</sup> <sub>-17.07</sub>	VRO
384	.....	-14.8	17.67 ± 0.03	4.34 ± 0.03	1.91 ± 0.03	1.95 ± 0.03	Burst	2.78	1.50 <sup>+0.30</sup> <sub>-0.14</sub>	0.50 <sup>+0.20</sup> <sub>-0.14</sub>	0.010 <sup>+0.027</sup> <sub>-0.010</sub>	Q1126+101 (SM1)
387	.....	-43.1	19.3	5.57 ± 0.21	2.18 ± 0.12	> 3.46	Const	5.54	1.85 <sup>+0.45</sup> <sub>-0.40</sub>	0.44 <sup>+0.23</sup> <sub>-0.23</sub>	2.75 <sup>+1.75</sup> <sub>-2.75</sub>	VRO
425	.....	-35.3	18.93 ± 0.05	6.18 ± 0.22	3.40 ± 0.20	> 2.72	Const	14.60	2.35 <sup>+0.60</sup> <sub>-0.25</sub>	0.55 <sup>+0.20</sup> <sub>-0.07</sub>	19.75 <sup>+0.25</sup> <sub>-17.45</sub>	VRO
447	.....	-26.1	19.38 ± 0.09	> 6.95	2.57 ± 0.13	2.88 ± 0.31	Burst	4.93	1.90 <sup>+0.40</sup> <sub>-0.25</sub>	0.75 <sup>+0.55</sup> <sub>-0.45</sub>	0.14 <sup>+1.14</sup> <sub>-0.14</sub>	ERO
520	.....	-33.4	19.30 ± 0.08	6.22 ± 0.30	2.18 ± 0.10	2.72 ± 0.19	Burst	2.50	0.70 <sup>+0.50</sup> <sub>-0.35</sub>	1.10 <sup>+0.45</sup> <sub>-0.45</sub>	0.32 <sup>+0.48</sup> <sub>-0.32</sub>	VRO
539	.....	-56.0	19.21 ± 0.09	> 7.04	1.69 ± 0.08	2.87 ± 0.19	Burst	6.21	1.40 <sup>+0.35</sup> <sub>-0.20</sub>	0.00 <sup>+0.12</sup> <sub>-0.00</sub>	20.00 <sup>+0.00</sup> <sub>-16.00</sub>	ERO

NOTES—Catalog ID is the identification number of the possible optical/near-IR counterpart(s) in our catalogs of these fields (available on request from the first author).  $\Delta\alpha$  and  $\Delta\delta$  are offsets in arcseconds from the quasar, with positive offsets to the north and east. Magnitudes are FOCAS total magnitudes; colors are FOCAS isophotal colors. All lower limits to colors are  $3\sigma$  limits. The model column gives the best fit of the two star formation histories we considered: an instantaneous burst ("Burst") or a constant star formation rate ("Const"), both with 20% solar metallicity. Ages are given in gigayears. In the notes column, ERO denotes  $r-K \geq 6.322$  and VRO denotes  $5.4 < r-K < 6.322$  (§ 7.3), red  $z-J$  denotes an object with  $z-J > 2.9$  but  $r-K < 6.322$  and  $J-K < 2.5$  (§ 7.3), and SCG denotes a member of the spatially compact group around Q0835+580 (§ 7.1.1).

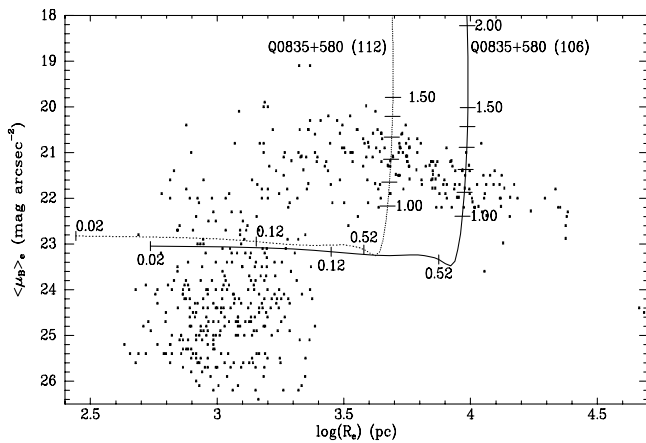


FIG. 7.—Redshift estimates for adaptive optics targets Q0835+580 (106) (solid line) and Q0835+580 (112) (dotted line) using the average rest frame  $B$ -band surface brightness-effective radius relation for giant elliptical galaxies. Labelled tick marks show the positions for various assumed redshifts, including every  $\Delta z = 0.1$  from  $z = 1$  to  $z = 1.5$ . Points are local ellipticals from Sandage & Perelmuter (1990). Both curves assume  $q_0 = 0.225$ . Assuming  $q_0 = 0.0$  (0.5) would make little difference at  $z \leq 0.52$ , but it would shift the vertical curves rightward (leftward) by  $\sim 0.1$  in the log by  $z = 2$ .

galaxies as indicated by their radial profiles, we can use the Kormendy relation between effective radius and average effective surface brightness (Kormendy & Djorgovski 1989) to determine what redshifts are consistent with the objects' observed sizes and surface brightnesses (Eisenhardt et al. 1996). To perform this analysis we use the elliptical colors and evolutionary and  $k$ -corrections of Poggianti (1997) and adopt their  $H_0 = 50$ ,  $q_0 = 0.225$  cosmology for consistency. For each redshift at which Poggianti (1997) calculate  $e$ - and  $k$ -corrections, we use the CFHT data to compute the rest-frame  $B$ -band surface brightness within  $r_e$  [accounting for  $(1+z)^4$  surface brightness dimming] and the physical size corresponding to the observed  $r_e$ . The tracks for both objects are shown in Figure 7 along with data for local ellipticals from Sandage & Perelmuter (1990). Both objects intersect the blue surface brightness-effective radius relation for ellipticals both at low and high redshift. Q0835+580 (112) could be at  $0.04 < z < 0.24$  or  $1 < z < 1.4$ , and Q0835+580 (106) could be at  $0.02 < z < 0.10$  or  $1 < z < 1.3$ . We compare these estimates with those from photometric redshifts in § 7.1.3.

#### 7. PHOTOMETRIC REDSHIFTS AND OTHER CONSTRAINTS FROM SED FITS

Estimating photometric redshifts  $z_{\text{ph}}$  and spectral types from multicolor photometry can provide insights into the nature of faint, high- $z$  objects which are otherwise too faint or too numerous for efficient spectroscopy (for a recent review see Yee 2000). In our RLQ fields we wish to quantitatively confirm or refute the existence of excess galaxies at or beyond the quasar redshifts and to investigate the SEDs—and hence the evolutionary state—of such galaxies, particularly EROs. A longer term goal is to provide an efficient way to reject contaminants foreground to the quasars in future spectroscopic follow-up studies. Currently, we have sufficient multicolor imaging data for such fitting in only the Q0835+580 and Q1126+101 fields.

An established technique for measuring photometric redshifts is to compare the photometry of objects of interest

with that of an *empirical* template set. This technique works well for galaxies with normal SEDs, where local template spectra (e.g., the set of Coleman, Wu, & Weedman 1980) provide good results even to high redshifts (e.g., Sawicki, Lin, & Yee 1997). However, because EROs are atypical objects, and potentially very dusty, it is inadvisable to fit their photometry with templates that are representative only of normal galaxies. Instead, it is important to allow for the possibility of heavy dust obscuration using synthetic templates reddened with a range of dust values.

We thus constructed a grid of models spanning a range in redshift, age, and reddening. The basis of this grid is the Bruzual & Charlot version (in Leitherer et al. 1996) of the spectral synthesis models of Bruzual & Charlot (1993), spanning 221 age steps  $0 \leq t \leq 2 \times 10^{10}$  yr. We considered instantaneous burst and continuous star formation models, which bracket the extremes of monotonically decreasing star formation histories. We assumed a metallicity of  $0.2 Z_{\odot}$ , though solar metallicity models were also considered for a subset of objects. Our synthetic spectra were attenuated using the Calzetti (1997) starburst galaxy extinction recipe, for a total of 67 values of  $E(B-V)$  spanning  $0 \leq E(B-V) \leq 2$ . The reddened spectra were then redshifted onto a grid of 101 redshifts spanning  $0 \leq z \leq 5$ , after which they were convolved with filter transmission curves to compute the final grid of galaxy colors as a function of redshift, reddening, and age.

The observed photometry for each object was compared with the model grids and the best-fitting position in  $z_{\text{ph}}$ , age,  $E(B-V)$  space was found by means of a maximum likelihood test. Almost all the input data used in these calculations was reported in HGC98. The exception is five hours of  $U$  imaging of the Q0835+580 field obtained with the Steward Observatory 90" on UT 1997 December 31 and reduced in the same manner as the data of HGC98. FOCAS total magnitudes were measured in all filters using apertures from the summed  $r+J+K_s$  image and converted to fluxes using the conversions in Appendix A of HGC98 plus that of Fukugita, Shimasaku, & Ichikawa (1995) for the  $U$  data.

Our procedure is thus similar to that used by Sawicki & Yee (1998) in their investigation of the spectral energy distributions of Lyman break galaxies. However, unlike in Sawicki & Yee (1998), where the redshifts of objects of interest were known a priori, here we must find the best-fitting model in the three-dimensional space that covers redshift, in addition to age and dust attenuation values.

For each object fit,  $\chi^2_{\nu}$  (reduced  $\chi^2$ ) contour plots with projected 90% confidence error contours in the  $z/E(B-V)$  and age/ $E(B-V)$  planes were constructed for each SFR scenario (Figs. 9–14 and Table 4). All our quoted uncertainties and plotted error bars are these projected 90% confidence limits. They are thus somewhat more conservative than the standard  $1\sigma$  (68% confidence) Gaussian error bars. It should also be kept in mind that the 90% confidence regions are typically not just elliptical Gaussians, but are elongated because of degeneracies between parameters such as age and  $E(B-V)$ . Plotting simple error bars, while convenient, thus tends to exaggerate the apparent uncertainties.

We define a successful fit as one where at most one of the three variables of interest— $z_{\text{ph}}$ ,  $E(B-V)$ , and age—is unconstrained at 90% confidence (i.e., that variable has 90% confidence limits equal to its range of permitted values). Note that a successful fit can still be a poor fit, with a high  $\chi^2_{\nu}$  value, and vice versa. There is a continuum of

properties across our dividing line between successful and unsuccessful fits, of course, but objects not successfully fitted typically have large photometric errors, which prevent their SEDs from usefully constraining the fitted parameters. However, unsuccessful fits can also be caused by star formation histories that deviate strongly from the instantaneous burst or continuous histories we consider, such as multiple strong bursts or slowly declining star formation rates.

In the following sections we present our photometric redshift results. In addition to fitting a handful of specific objects of interest, we examine a compact clump of predominantly red galaxies around Q0835+580 to confirm or refute the visual impression that these galaxies are associated with the quasar. We also examine the population of very red galaxies in these fields regardless of their distance from the RLQ, because these galaxies may be part of extended structures at the quasar redshift. Furthermore, these red objects may be dusty starbursting galaxies or high-redshift galaxies with old stellar populations, both of which are of great interest to the study of galaxy evolution.

### 7.1. Q0835+580 Field

The field of Q0835+580 has data in seven filters (*UrizJHK*) for most objects. As discussed above, we do not compute  $z_{\text{ph}}$  values for all galaxies in the field, but instead focus in the following sections on specific galaxies or galaxy populations.

#### 7.1.1. The Spatially Compact Group Around Q0835+580

There are 18 objects within  $21''.5$  of Q0835+580 to  $K = 21.24$  (the  $5\sigma$  limit of our data) which form a spatially compact group in the terminology of Stanford et al. (1997). This count excludes the quasar, one bright morphologically classified star, and one probable star which is unresolved on an *HST* WFPC2 snapshot image. As discussed in HG98 (see their Fig. 23), the compact spatial distribution of these galaxies and the red color of many of them makes it very likely that they are at the redshift of the quasar ( $z_q = 1.5358$ ) or the intervening Mg II systems ( $z \simeq 1.4368$ ).

To test this hypothesis, we have fitted the broadband magnitudes of these 18 objects. They are denoted “SCG” in the notes column of Table 4, which summarizes the fit results. All objects had successful fits, as defined in the pre-

vious section. Figure 8a shows  $E(B-V)$  versus  $z_{\text{ph}}$  (at the best-fit model age) for the twelve objects with  $K \leq 20$  (*large symbols*) and the six with  $K > 20$  (*small symbols*). Figure 8b shows the best-fit model age versus  $z_{\text{ph}}$ . Instantaneous bursts (*squares*) are preferred over constant star formation histories (*triangles*) in nine of 12 cases at  $K \leq 20$ , but only two of six cases at  $K > 20$ . Figure 8b shows the best-fit model age versus  $z_{\text{ph}}$ . The dotted vertical line in both figures shows the quasar redshift. Recall that the simple error bars we plot for convenience do exaggerate the uncertainties somewhat.

Twelve of the 18 objects are consistent with being at the quasar redshift at 90% confidence. Another, which misses being consistent by  $\Delta z = 0.06$ , is coincident with the southern radio hot spot of the quasar (see § 7.2 of HG98), so we consider it to be at the quasar redshift as well. Thus there is good evidence from photometric redshifts for galaxy overdensities at the quasar redshifts. For these 13 galaxies the typical  $E(B-V)$  is  $\sim 0.3$  and the typical fitted age is  $\sim 1$  Gyr. Both quantities have large uncertainties, and there is a large scatter in the ages. Nonetheless, overall the plots are consistent with current or recent star formation in the majority of the galaxies at the quasar redshifts, as denoted by a best-fit constant star formation history or a best-fit age of  $< 1$  Gyr.

The notable exception to this is Q0835+580 (339), which is a bright ERO with  $r-K > 7$  best fit by an instantaneous burst with  $z_{\text{ph}} = 1.65^{+0.20}_{-0.30}$ ,  $E(B-V) = 0.00^{+0.20}_{-0.00}$ , and age  $19.75^{+0.25}_{-13.00}$  Gyr (Fig. 9a). Four other objects have similar best-fit ages which are older than the universe at the quasar redshift for all reasonable cosmologies, but this is the only one for which even the 90% confidence lower limit on the age is older than the universe. For reference, note that for the current best-fit flat, low- $\Omega_M$ , nonzero  $\Omega_\Lambda$  cosmology, at  $z = 1.5$  the age of the universe was  $(4.7^{+1.7}_{-0.8}) h_{75}^{-1}$  Gyr ( $\Omega_M = 0.2 \mp 0.1$ ,  $\Omega_\Lambda = 1 - \Omega_M$ ). To see whether we have overestimated this object’s age by underestimating its metallicity, we refitted it using solar metallicity models. Both solar metallicity fits have lower  $\chi^2_\nu$  than 20% solar fits, though the instantaneous burst is again preferred (Fig. 9b), with slightly lower values of all three main parameters:  $z_{\text{ph}} = 1.40^{+0.20}_{-0.20}$ ,  $E(B-V) = 0.00^{+0.04}_{-0.00}$ , and age  $12.5^{+7.5}_{-8.0}$  Gyr. The 90% confidence lower limit on the age for even this solar metallicity

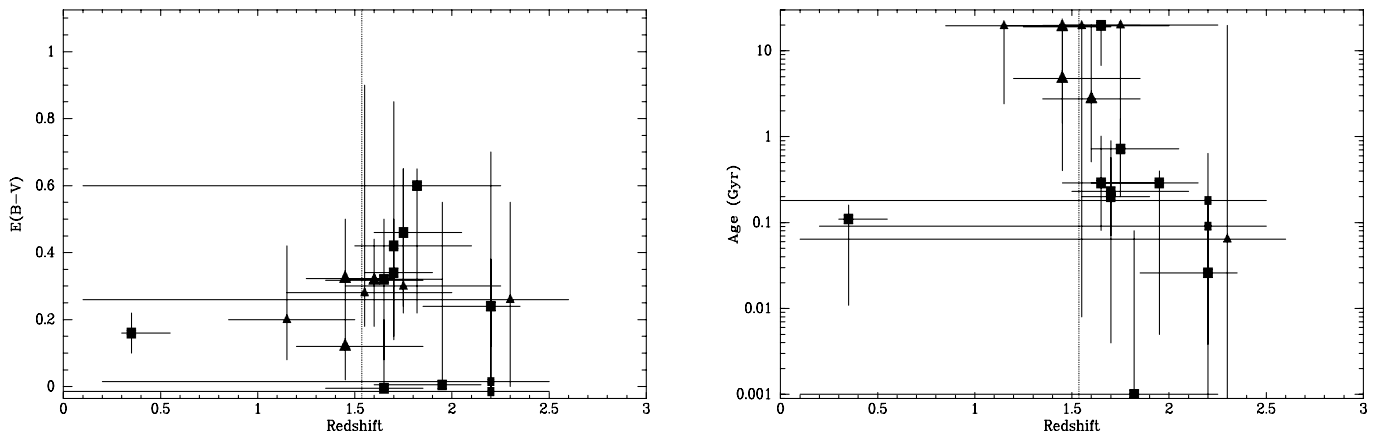


FIG. 8.—Left:  $E(B-V)$  vs.  $z_{\text{ph}}$  for the best-fit model of 12 objects with  $K \leq 20$  (*large symbols*) and six with  $K > 20$  (*small symbols*) within  $21''.5$  of Q0835+580. Instantaneous bursts (*squares*) are preferred over constant star formation histories (*triangles*) in nine of 12 cases at  $K \leq 20$  but only two of six cases at  $K > 20$ . The vertical dotted line shows the quasar redshift. The error bars are projected 90% confidence limits (see text). Objects with  $E(B-V) = 0$  have been arbitrarily offset by small amounts in  $E(B-V)$  to show the error bars. Right: Age vs.  $z_{\text{ph}}$  for the same objects.

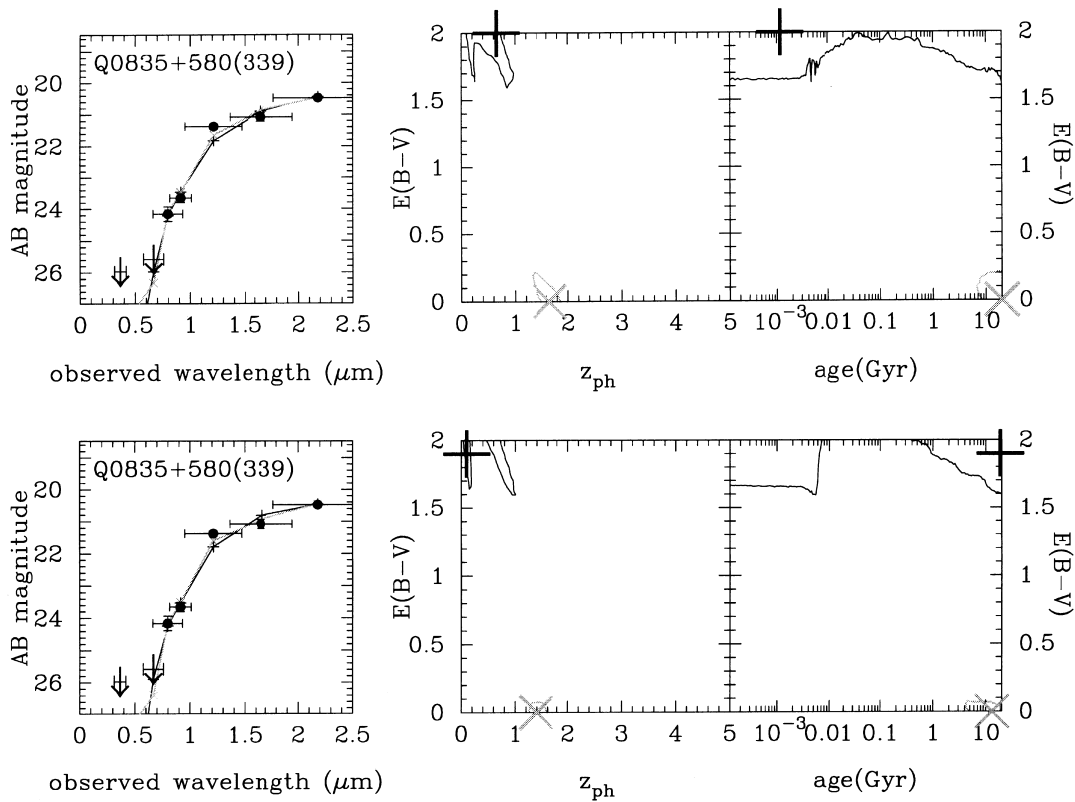


FIG. 9.—SED-fitting results for ERO Q0835+580 (339). *Top*: 20% solar metallicity fit. *Bottom*: solar metallicity fit. In each plot, the left panel shows the observed flux points and the best-fit SED points connected by straight line segments. In all panels, the two different star formation histories we modeled are denoted by lines of different colors: gray for an instantaneous burst and black for a constant star formation rate. The middle and right panels are two perpendicular projections of the three-dimensional space of  $E(B-V)$ ,  $z$ , and age. In each of these two panels, the cross and the plus sign mark the best-fit values for instantaneous burst and constant star formation models, respectively, while the contours show the projection of the 90% confidence volume.

fit is still older than the age of the universe at the quasar redshift, except for flat  $\Lambda$ -dominated cosmologies with  $\Omega_M \leq 0.2$ . Thus, even though higher metallicities may further reduce the best-fit age, Q0835+580 (339) is clearly worthy of spectroscopic study as a candidate very old galaxy at high redshift.

Another of the objects within  $21''5$  of the quasar, Q0835+580 (352), is known to be at  $z = 0.236$  (Burbidge et al. 1990), which provides a useful check of the accuracy of our photometric redshifts. The object is confused with a separate red galaxy (Fig. 23 of HG98) which contributes negligible flux in  $U_{\text{rizz}}$  but  $\sim 0.5$  mag in  $J$  and  $H$  and  $\sim 0.25$  mag in  $K$ . Our fit to its corrected photometry yields  $z_{\text{ph}} = 0.35^{+0.20}_{-0.05}$  and  $E(B-V) = 0.16 \pm 0.06$ . This redshift is only  $2.3 \sigma$  above the known redshift, and this  $E(B-V)$  value is close to the average value of  $\simeq 0.1$  estimated for field galaxies at  $\langle z \rangle = 0.3$  (Lin et al. 2001). We thus consider our fit to be acceptable.

### 7.1.2. Q0835+580 (H $\alpha$ 1)

The object Q0835+580 (398) is also known as Q0835+580 (H $\alpha$ 1), a candidate H $\alpha$  emitter at the quasar redshift (§ 4). However, it is best fitted as a young  $z_{\text{ph}} \simeq 2.15 \pm 0.25$  galaxy with  $E(B-V) \simeq 0.35 \pm 0.20$  under either the single stellar population or constant SFR models, although a similarly reddened object at  $z_{\text{ph}} \sim 0.25$  is also possible at 90% confidence. We also fitted this object using solar metallicity models and found that the best-fit redshift did not change significantly, though the best-fit reddening was somewhat lower,  $E(B-V) \simeq 0.20 \pm 0.20$ , and only the con-

stant SFR model still permitted a low-redshift ( $z_{\text{ph}} \sim 0.2$ ) solution at 90% confidence. It is possible that the narrow-band filter detected [O III]  $\lambda 5007$  at  $z = 2.3338 \pm 0.0186$  instead of H $\alpha$  at  $z = 1.5358$ , but the  $z_{\text{ph}} \sim 0.25$  option would be impossible to reconcile with the narrowband detection. Spectroscopy is needed in this case to verify the photometric redshift.

### 7.1.3. Q0835+580 Field Adaptive Optics Targets

Photometric redshifts were computed for Q0835+580 (106) and (112) for comparison with the structural redshifts calculated for these objects from adaptive optics images (§ 6). The direct SED fits do not agree very well with the structural redshifts. Figure 10a shows that Q0835+580 (106) is best fit as a  $z_{\text{ph}} = 4.50 \pm 0.15$  galaxy with  $E(B-V) \simeq 0.23^{+0.25}_{-0.18}$ . The structural redshift of  $z \simeq 0.8$  is excluded at high confidence for the models considered. This result supersedes the earlier modeling attempt reported in Hall, Sawicki, & Lin (2000). Figure 10b shows that Q0835+580 (112) is not well fitted by any of our simple models ( $\chi^2 \simeq 20$ ). A composite stellar population may improve the fit, but that may cast some doubt on its morphological identification as an early-type galaxy. From comparison of Figures 10–14, as well as similar plots for other objects (not shown), it appears that the  $r_{\text{izz}}$  fluxes for these two objects, especially Q0835+580 (112), are unusually bright relative to the  $U$  and  $JHK$  fluxes, even compared with blue objects. Thus we believe the reason for the poor SED fits to these objects is that their  $r_{\text{izz}}$  photometry is affected by scattered light from the nearby adaptive

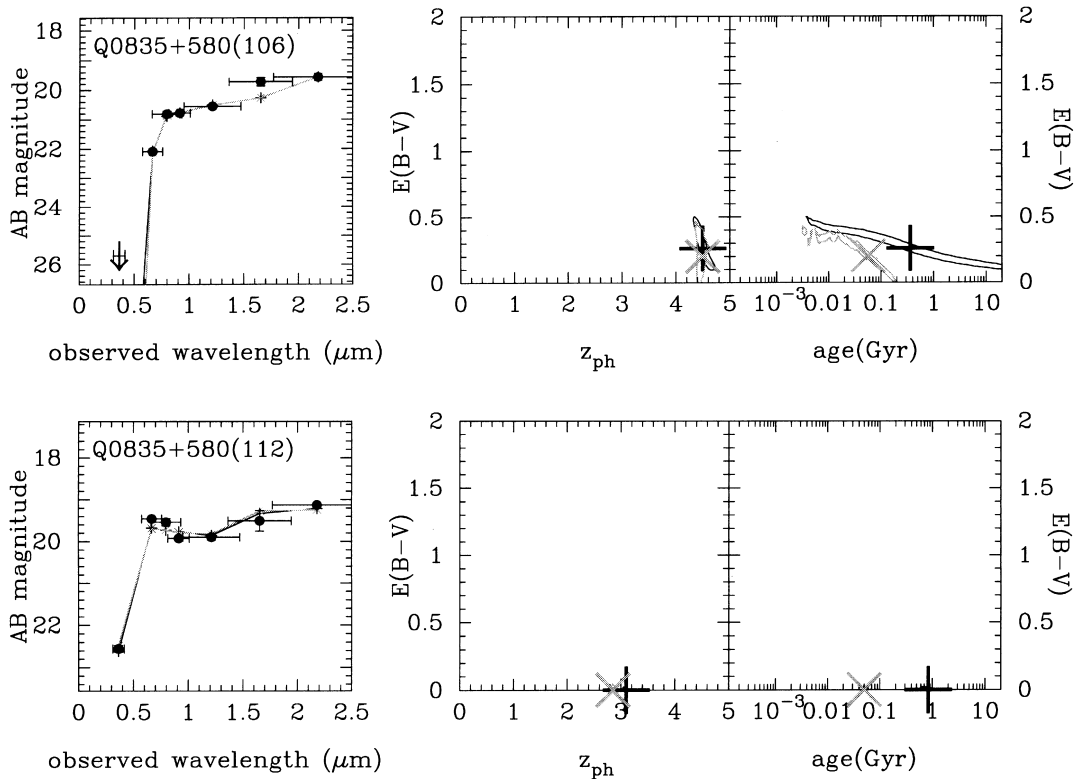


FIG. 10.—SED-fitting results for adaptive optics targets. *Top*: Q0835 + 580 (106). *Bottom*: Q0835 + 580 (112). See Fig. 9 for details.

optics guide star, despite attempts to account for such light through masking, subtracting, and using local backgrounds. Multiwavelength adaptive optics imaging may be necessary to obtain accurate photometry for further study of these objects.

#### 7.1.4. Q0835 + 580 Field Possible Submillimeter Counterparts

Q0835 + 580 (117) and (458) were chosen for SED fitting since they are possible counterparts of tentative submillimeter detections (§ 5). Figure 11a shows that Q0835 + 580 (117) is best fitted as an instantaneous burst with  $E(B-V) = 0^{+0.12}_{-0.00}$  at a redshift consistent with that of the quasar ( $z_{\text{ph}} = 1.60 \pm 0.15$ ). A constant star formation history requires  $E(B-V) = 0.20^{+0.14}_{-0.16}$  and is also consistent with the quasar redshift, though with larger uncertainties. Neither fit provides evidence for extreme dust reddening as might be expected for a submillimeter-detected galaxy, and neither does a fit using solar metallicity spectral templates. Thus the identification of Q0835 + 580 (117) with Q0835 + 580 (SM1) is doubtful. However, such simple positional identifications of optical counterparts to submillimeter sources are not expected to be extremely robust given the 14" FWHM of the SCUBA beam at 850  $\mu\text{m}$ .

Figure 11b shows that Q0835 + 580 (458) is best fitted as an instantaneous burst at  $z_{\text{ph}} = 1.2^{+0.2}_{-0.1}$  with  $E(B-V) = 0.55^{+0.15}_{-0.05}$ , though a constant star formation history at  $z_{\text{ph}} = 1.35^{+0.10}_{-0.15}$  with the same reddening is also acceptable. This galaxy's photometric redshift, which places it slightly foreground to the quasar, is consistent with it being slightly brighter than expected for a brightest cluster galaxy at the quasar redshift. Its high  $E(B-V)$  is consistent with it being

the counterpart of Q0835 + 580 (SM2). This possible luminous submillimeter-detected starburst at (or nearly at) the quasar redshift clearly warrants spectroscopic follow-up.

## 7.2. Q1126 + 101 Field

The field of Q1126 + 101 ( $z_q = 1.5173$ ) has data in five filters (*rzJHK*) for most objects, and we can only fit objects with data (including upper limits) in all filters. There is no distinct spatially compact group of galaxies around Q1126 + 101 as there is around Q0835 + 580. However, there is a nearby clump of *J-K*-selected EROs which may be galaxies background to the quasar or very dusty galaxies at the quasar redshift (discussed in § 7.2.2), as well as a population of *R-K*-selected EROs which may be old galaxies in an overdensity at the quasar redshift (discussed in § 7.3). First, however, we discuss a possible submillimeter source identification.

### 7.2.1. Q1126 + 101 Field Possible Submillimeter Counterpart

Q1126 + 101 (384) was chosen for SED fitting since it is a possible counterpart of submillimeter source Q1126 + 101 (SM1) (§ 5). The best fit ( $\chi^2 = 2.78$ ) is an instantaneous burst with  $z_{\text{ph}} = 1.50^{+0.30}_{-0.15}$  and  $E(B-V) = 0.50^{+0.20}_{-0.14}$  (Fig. 12); the constant SFR fit also requires a large  $E(B-V) = 0.55^{+0.20}_{-0.11}$ . These large  $E(B-V)$  values support the idea that Q1126 + 101 (384) is the optical counterpart of the SCUBA source in this field. The galaxy has  $K = 17.7$ , making it  $\sim 0.4$  mag brighter than the magnitude of a brightest cluster galaxy at the quasar redshift as estimated by HG98, but it is within the observed scatter in such objects' magnitudes at  $z \simeq 1$  (Thompson, Aftreth, & Soifer 2000). As with Q0835 + 580 (458), this possible luminous submillimeter-

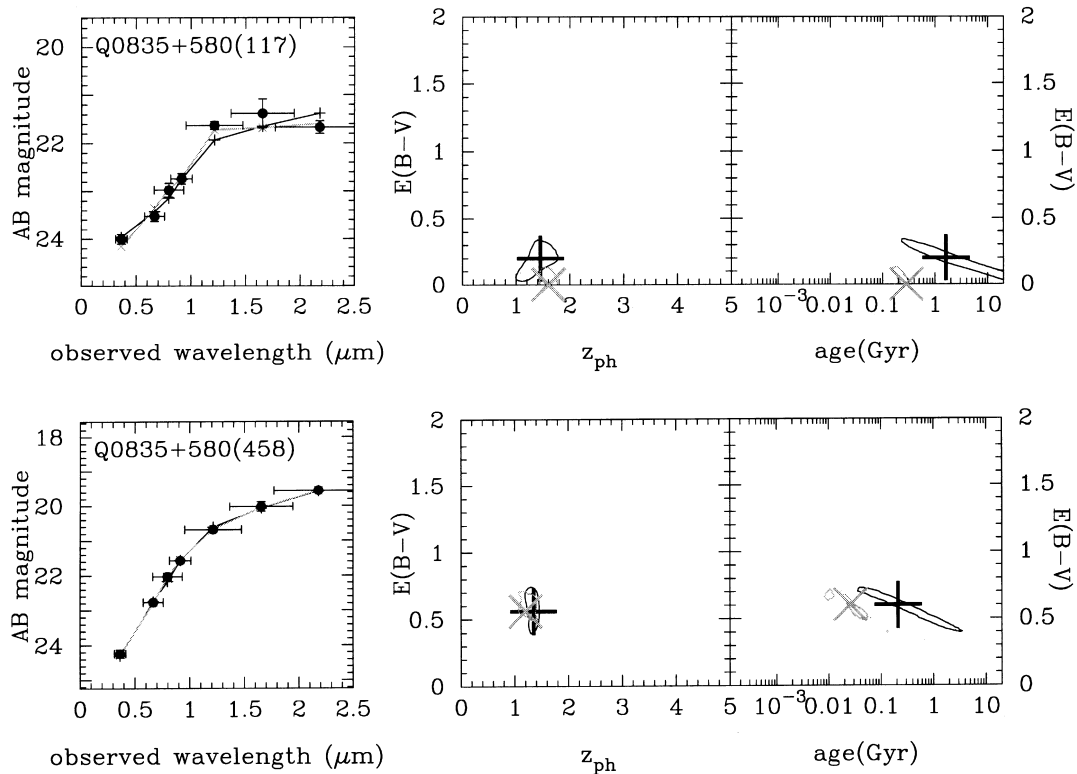


FIG. 11.—SED-fitting results for candidate submillimeter source counterparts in the Q0835+580 field. *Top*: Q0835+580 (117). *Bottom*: Q0835+580 (458). See Fig. 9 for details.

detected starburst at the quasar redshift clearly warrants spectroscopic follow-up.

### 7.2.2. Q1126+101 Field $J-K$ -selected EROs

Four of the brightest  $J-K$ -selected EROs in the Q1126+101 field had data sufficient for SED fitting. Figure 13 shows the best fit of these, Q1126+101 (447) and Q1126+101 (424). Q1126+101 (447) is best fitted as a dusty instantaneous burst consistent with the quasar redshift ( $z_{\text{ph}} = 1.9^{+0.4}_{-0.5}$  and  $E(B-V) = 0.75^{+0.55}_{-0.45}$ ). Q1126+101 (424) is best fitted as a less dusty, constant SFR model background to the quasar at  $>99.9\%$  confidence ( $z_{\text{ph}} = 3.00^{+0.95}_{-0.40}$  and  $E(B-V) = 0.46^{+0.24}_{-0.10}$ ). This agrees with our suggestion in § 7.3 of HG98 that it is an example of a dusty star-forming galaxy at  $z \gtrsim 2.5$ , with the 4000 Å break in  $J$  or beyond.

The other two  $J-K$ -selected EROs we fitted were Q1126+101 (381), which has very red  $z-J > 3.4$ , and Q1126+101 (425), the brightest  $J$ -band dropout in the field.

In HG98 we suggested that these were examples of dusty star-forming galaxies at the quasar redshift  $z_q = 1.5173$ , which puts the 4000 Å break between  $z$  and  $J$ . Figure 14 shows that both of these objects are best fitted with highly reddened constant SFR models (though for Q1126+101 (381) an instantaneous burst is almost as good) background to the quasar at almost exactly 90% confidence. Q1126+101 (381) has  $z_{\text{ph}} = 1.95^{+0.45}_{-0.35}$  and  $E(B-V) = 0.55^{+0.40}_{-0.11}$ . Q1126+101 (425) has  $z_{\text{ph}} = 2.35^{+0.60}_{-0.25}$ , and  $E(B-V) = 0.55^{+0.20}_{-0.07}$ . This  $z_{\text{ph}}$  for Q1126+101 (425) is slightly lower than the value of  $z_{\text{ph}} = 3.5 \pm 0.5$  reported in Hall et al. (1999) based on earlier modeling, but the  $E(B-V)$  is the same within the uncertainties. The fits for both objects have large  $\chi^2_{\nu}$  values because they underpredict the flux in the  $r$  band, and the same is true to a lesser extent for Q1126+101 (424). This may represent a limitation of our simple models with uniform  $E(B-V)$ . The addition of a small amount of unreddened light from a young stellar

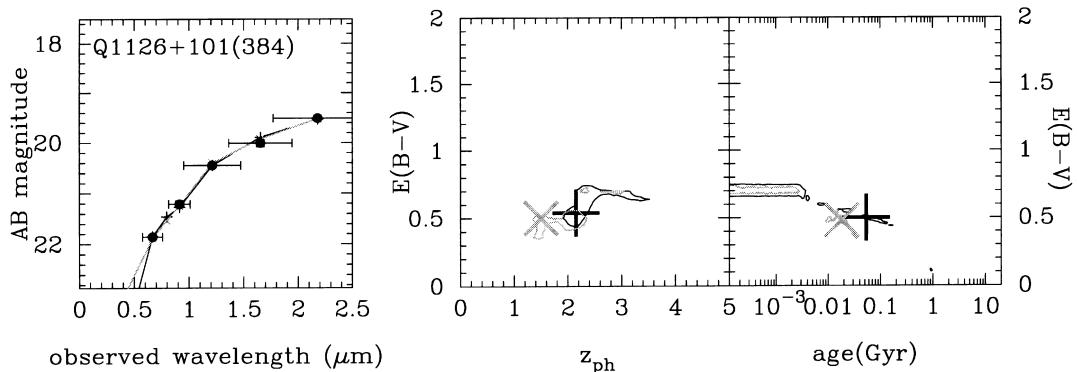


FIG. 12.—SED-fitting results for candidate submillimeter source counterpart Q1126+101 (384). See Fig. 9 for details.

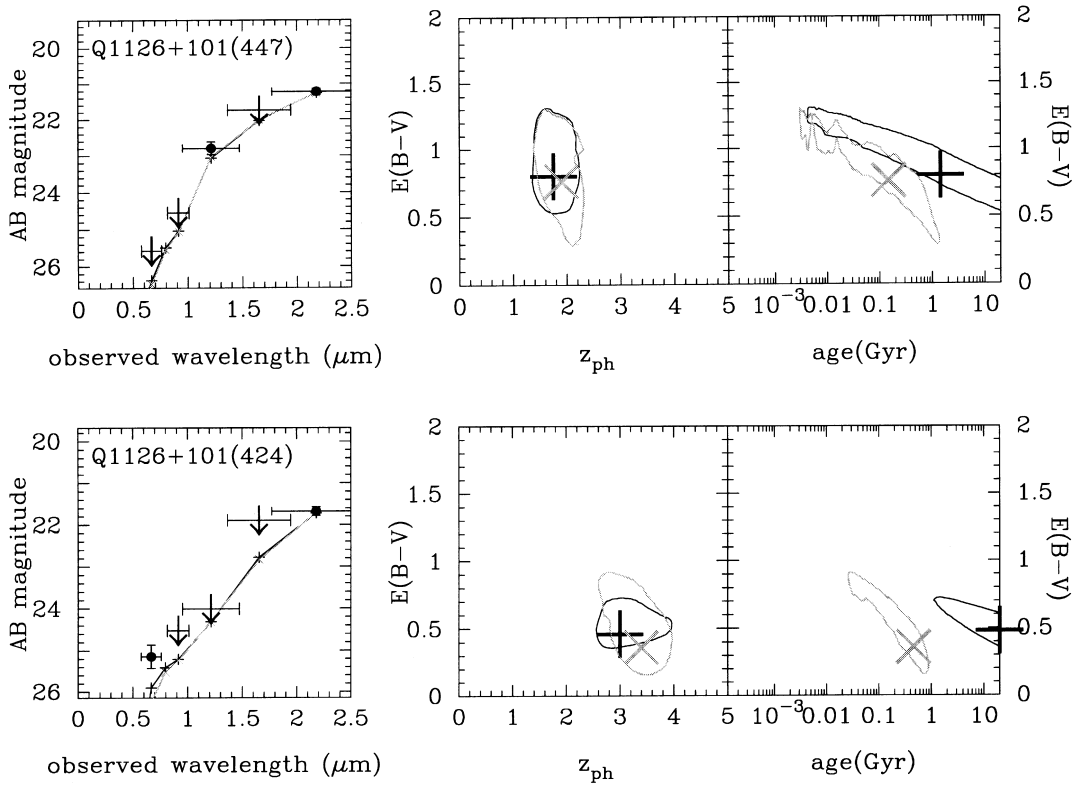


FIG. 13.—SED-fitting results for  $J-K$ -selected EROs. *Top*: Q1126+101 (447). *Bottom*: Q1126+101 (424). See Fig. 9 for details.

population could bring the fits into agreement with the  $r$ -band data while not destroying their agreement with the observed fluxes at longer wavelengths (see HG98).

As mentioned in HG98, the large  $E(B-V)$  values for these objects are consistent with their  $J-K$  colors being

comparable to, or redder than, the prototypical dusty ERO HR10, which requires dust reddening to fit its SED at its known  $z = 1.44$  in any reasonable cosmology (Hu & Ridgway 1994; Graham & Dey 1996; Cimatti et al. 1997). However, the prediction of HG98 that Q1126+101 (381)

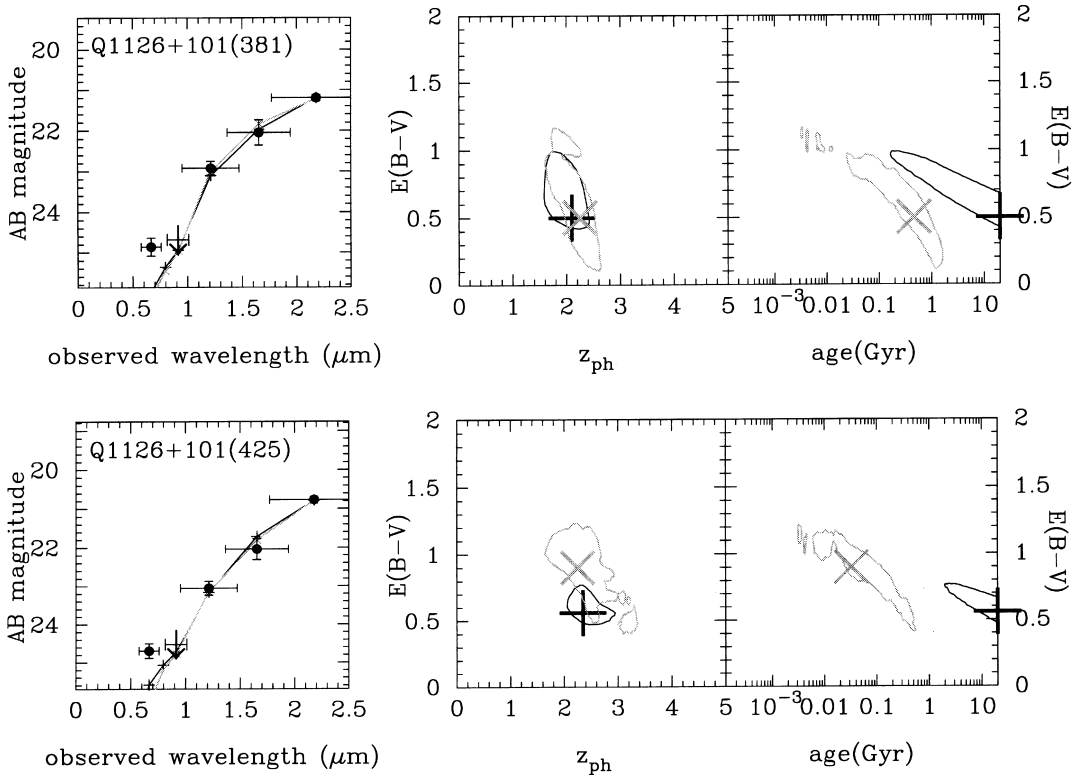


FIG. 14.—SED-fitting results for  $J-K$ -selected EROs. *Top*: Q1126+101 (381). *Bottom*: Q1126+101 (425). See Fig. 9 for details.

and Q1126+101 (425) would be at the quasar redshift seems erroneous based on their photometric redshifts, though the quasar redshift is excluded at only 90% confidence. The  $z_{\text{ph}}$  of these objects are plausible in the sense that their  $K$  magnitudes would be fainter than those of powerful radio galaxies (typically the brightest galaxies at any redshift) at the same redshifts (van Breugel et al. 1998). Their being background to the quasar is also consistent with the lack of a strong concentration of excess galaxies around the quasar on the sky in this field (§ 2.3). We also fitted solar metallicity models to these four objects to see if their  $E(B-V)$  values or redshifts depended strongly on metallicity. The fits were of comparable but slightly worse  $\chi^2_{\nu}$  on average, and none of the best-fit redshifts or  $E(B-V)$  values changed enough to affect our conclusions.

In summary, fits to the SEDs of these four  $J-K$ -selected EROs all require strong reddening, with  $E(B-V)$  values of  $\sim 0.6 \pm 0.3$ . Two are better fitted by constant SFR models, while two have nearly identical  $\chi^2_{\nu}$  for either constant SFR or instantaneous burst models. The best-fit photometric redshifts are  $1.9 \leq z_{\text{ph}} \leq 3$ , and only Q1126+101 (447) is consistent with being at the quasar redshift at 90% confidence. Small amounts of unreddened light from a young stellar population are needed to match the  $r$ -band data for all three of the  $z_{\text{ph}} > z_q$  objects. All these conclusions hold for both solar and 20% solar metallicity templates. These  $J-K$ -selected EROs may be representative of a population of dusty and star-forming galaxies missing from optically selected samples.

### 7.3. Very Red Objects and Extremely Red Objects

Photometric redshifts were also computed for all objects with  $r-K > 5.4$  and  $K < 19.6$  in both fields. Such objects could be old stellar populations at high redshift or dusty starbursting galaxies, both populations of great interest to the study of galaxy evolution. Objects with  $r-K > 5.4$  but  $r-K < 6.322$  are not red enough to meet our definition of an ERO, but objects with  $r-K > 5.322$  are called EROs by Cimatti et al. (1999) and Daddi et al. (2000), and objects with  $r-K > 5.622$  are called EROs by Pozzetti & Mannucci (2000) and Martini (2001). To avoid confusion with our definition of EROs we refer to objects with  $5.4 < r-K < 6.322$  as very red objects (VROs; see Cohen et al. 1999). There are 12 such objects in the Q0835+580 field, one of which was not successfully fitted. Excluding two

objects with the colors of late-M or L dwarf stars (see Hall 1998), there are 12 VROs in the Q1126+101 field with sufficient photometric data for fitting, one of which was not successfully fitted. Overall, in both fields, we successfully fitted 22  $r-K > 5.4$  objects with  $K < 19.6$ .<sup>17</sup> These 22 objects include four from the spatially compact group discussed in § 7.1.1 and three of the four  $J-K$ -selected EROs discussed in § 7.2.2. One of these 22, Q1126+101 (91), is best fitted as a  $\lesssim 0.2$  Gyr old instantaneous burst with  $E(B-V) = 0.6 \pm 0.2$  at  $z_{\text{ph}} = 5.0 \pm 0.3$ . If this is correct, with  $K = 19.5$  it would be one magnitude brighter than the  $z = 5.19$  radio galaxy TN J0924-2201 (van Breugel et al. 1999), but consistent with the scatter seen in the  $K-z$  relation at  $1 < z < 3$ . Thus this  $z_{\text{ph}}$  is not impossible, though it is unlikely. In this section we discuss only the remaining 21 of 22 very or extremely red objects, which all have  $1 \lesssim z_{\text{ph}} \lesssim 2$ .

Figure 15a plots  $E(B-V)$  versus  $z_{\text{ph}}$  for these 21 objects, and Figure 15b plots age versus  $z_{\text{ph}}$ . The distribution of  $E(B-V)$  values, and to a lesser extent the distribution of ages, are both skewed to slightly larger values than in Figure 8, with median  $E(B-V) \sim 0.4$  instead of  $\sim 0.25$  and median age  $\sim 0.7$  Gyr instead of  $\sim 0.3$  Gyr. Both trends are understandable since the objects in Figure 8 were chosen only for their proximity to the quasar, while those in Figure 15 were chosen on the basis of their red colors. Figure 15 also shows that there are more objects consistent (at the 90% confidence level) with the quasar redshift in the Q0835+580 field (*open squares*) than in the Q1126+101 field (*filled squares*). This is expected, since many of the Q1126+101 field objects are  $J-K$ -selected EROs, and at least some of that population is not expected to be at the quasar redshift (§§ 2.3 and 7.2.2).

Following Pozzetti & Mannucci (2000), we plot these 21 objects on an  $r-K$  versus  $J-K$  color-color diagram to study the separation of unreddened and reddened galaxies

<sup>17</sup> The two unsuccessfully fitted objects are Q0835+580 (618) and Q1126+101 (50). Q0835+580 (618) has  $z_{\text{ph}} < 0.9$  at 90% confidence, but its age and  $E(B-V)$  are unconstrained, since the SED can be fitted either as an extremely red  $z < 0.5$  galaxy and an unreddened  $z \sim 1.5$  galaxy. We suspect Q1126+101 (50) could not be fitted because of its red  $r-z$  and blue  $z-J$  colors, which can probably be simultaneously fitted only by a solar metallicity model at  $z \sim 1$ .

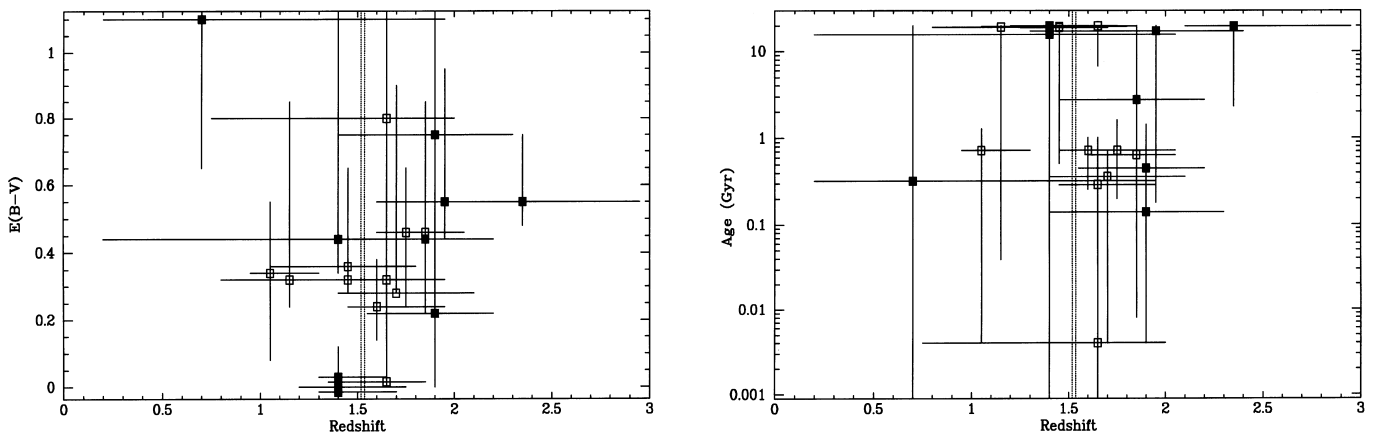


FIG. 15.—Left:  $E(B-V)$  vs.  $z_{\text{ph}}$  for all successfully fitted objects with  $r-K > 5.4$  and  $K < 19.6$  in the fields of Q0835+580 (*open squares*) and Q1126+101 (*filled squares*). The dotted vertical lines show the quasar redshifts. The error bars are projected 90% confidence limits (see text). Right: Age vs.  $z_{\text{ph}}$  for the same objects.

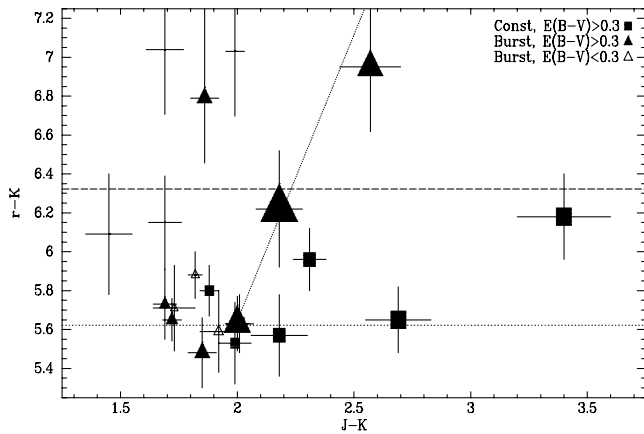


FIG. 16.— $r-K$  vs.  $J-K$  for all successfully fitted objects with  $r-K > 5.4$  and  $K < 19.6$  in the fields of Q0835+580 and Q1126+101 (see Table 4). Triangles denote objects for which instantaneous burst models are the best fits, and squares objects for which constant SFR models are best. Filled symbols denote  $E(B-V) > 0.3$ , and open symbols best-fit  $E(B-V) < 0.3$ . Note that all constant SFR models have best-fit  $E(B-V) > 0.3$ . The symbol sizes scale linearly with  $E(B-V)$ , with the largest best-fit value being 1.1. Objects without symbols are all best fitted as  $E(B-V) = 0$  bursts. Error bars extending off the plot indicate  $3\sigma$  lower limits on the  $r-K$  or  $J-K$  colors. Objects above the dashed line are EROs by our definition ( $R-K > 6$ , using  $r = R + 0.322$ ). The dotted lines show the elliptical (top left quadrant) and dusty starburst (top right quadrant) regions defined by Pozzetti & Mannucci (2000), again using  $r = R + 0.322$ . Our SED-fitting results indicate that their criteria are not as robust as might be hoped.

at  $1 \lesssim z_{\text{ph}} \lesssim 2$  (see also Martini 2001). Figure 16 shows that most objects' fits require dust reddening of  $E(B-V) > 0.3$  [filled symbols, with symbol size scaling linearly with  $E(B-V)$ ]. The separation of reddened and unreddened galaxies (open symbols) is not as clean as predicted by the modeling of Pozzetti & Mannucci (2000) for objects at  $1 < z < 2$ . Our modeling is very similar to that of Pozzetti & Mannucci (2000), but we fit a wider range of ages and  $E(B-V)$  values and use information from more filters than just  $RJK$  or  $IJK$ . In particular, they do not consider reddened instantaneous burst models, which we find are the best fits for many of our objects. Larger samples plus spectroscopic redshifts and spectral types are clearly desirable to calibrate this classification system. For now, we note that the general trend of objects with larger  $E(B-V)$  being redder in  $J-K$  is valid, but that this trend is not accurately predictive on an object by object basis.  $E(B-V) = 0$  objects may be an exception, since they seem to occupy a distinct region of the diagram with little contamination.

We also note that our results may differ from those of Moriondo, Cimatti, & Daddi (2000), who assembled *HST* images of a heterogeneous sample of VROs and EROs in both blank and candidate high-redshift cluster fields. They found that VROs and EROs with irregular morphologies, which are likely to include a higher percentage of star-forming galaxies than objects with regular morphologies, tend to have redder  $R-K$  or  $I-K$  colors. We may be able to compare these irregular EROs with objects in our sample which have large best-fit  $E(B-V)$  values, which also should include a higher percentage of star-forming galaxies than galaxies with low reddenings. As seen in Figure 16 and discussed above, we find that objects with large reddening do not tend to have redder  $r-K$  colors, although they do

tend to have redder  $J-K$  colors. Our heavily reddened EROs and the irregular EROs of Moriondo, Cimatti, & Daddi (2000) may be different populations, of course, but it would be very interesting if they were in fact comparable. In that case this result would indicate a breakdown in the relationship between morphology and star formation properties at  $z \gtrsim 1$ ; for example, if we are seeing irregular galaxies with relatively old or quiescent stellar populations and young or actively star-forming galaxies with nonetheless regular morphologies.

To test the sensitivity of our fits to metallicity, we refitted 16 objects using solar metallicity models instead of 20% solar ones. These solar fits had comparable  $\chi_v^2$ , with a tendency toward worse fits on average. Best-fit redshifts and  $E(B-V)$  values were unaffected by the different metallicity, with no discrepancies at  $>90\%$  confidence. Best-fit ages were found to be more sensitive to the metallicity, but even so, only in five cases where the solar metallicity fits had lower  $\chi_v^2$  did the best-fit ages change (decrease) at  $\gtrsim 90\%$  confidence. All five cases are best-fit instantaneous bursts, and four are  $E(B-V) = 0$  objects. This is consistent with our  $E(B-V)$  values being essentially the same for solar and 20% solar metallicity fits; the majority of our objects require dust for both metallicities, while a minority do not require it for either metallicity.

Finally, we attempted to fit four objects with  $z-J > 2.9$ , suggestive of a spectral break near  $1 \mu\text{m}$ , which have neither  $r-K > 5.4$  nor  $J-K > 2.5$ . One object—Q1126+101 (253)—was not successfully fitted due to its detection only in  $J$  and  $K$ . The three successfully fitted objects are denoted “red  $z-J$ ” in the notes column of Table 4, which summarizes the fit results. Q0835+580 (343) and (379) have fits similar to those of VROs and EROs. The  $r-K > 5.4$  definition of a VRO is somewhat arbitrary, and these two red  $z-J$  objects have  $r-K \simeq 5$ , so the similarity of their fits to those of VROs is not surprising. Q1126+101 (269) also has a best fit similar to those of VROs or EROs, but it has a large  $\chi_v^2$  value. We believe this is because it has only a moderately red color  $r-K = 4.4$ , which our simple stellar population models have trouble fitting simultaneously with this object's very red  $z-J > 3.7$ . A higher metallicity model with a slight contribution from an unreddened young population is probably needed to improve the  $\chi_v^2$  for this object.<sup>18</sup>

In summary, we have performed SED fits to a sample of red objects with a high a priori probability of having strong dust reddening or old stellar populations. Many of these objects' SED fits yield photometric redshifts consistent with the quasar redshifts. We find that significant dust is required to fit most of these objects, including about half of those which also require old ages. Our fits have  $E(B-V)$  values ranging from 0 to 1.1, with median  $E(B-V) \sim 0.4$ . For comparison, Lin et al. (2001) find an average  $E(B-V) \simeq 0.1$  from fitting the luminosity density evolution of  $z < 0.65$

<sup>18</sup> This object is one of seven in Table 4 with  $\chi_v^2 \gtrsim 10$ . Two others were discussed in § 7.2.2; they also require a contribution from an unreddened young population to fit the observed SED. Of the remaining four, Q0835+580 (307) probably requires both a metallicity  $> 0.2 Z_{\odot}$  and a young spectral component, while Q0835+580 (280) and (410) probably require only metallicities  $> 0.2 Z_{\odot}$ , and Q0835+580 (66) is definitely better fitted by a solar metallicity model. It is encouraging that the high  $\chi_v^2$  of all seven objects can be understood as due to limitations of our modeling.

field galaxies from the CNOC2 redshift survey, Thompson, Weymann, & Storrie-Lombardi (2000) find a distribution  $E(B-V) \leq 0.6$ , albeit peaked at  $E(B-V) \leq 0.1$ , for  $z < 2$  galaxies in the deep NICMOS image of the HDF-N, and Hammer et al. (2001) find  $E(B-V) \leq 1$ , peaked at  $E(B-V) \sim 0.5$ , for a sample of luminous compact galaxies at  $z \sim 0.65$ . Our  $E(B-V)$  values do not change significantly when we fit solar metallicity models instead of 20% solar models. However, the best-fit ages for the four objects with best-fit  $E(B-V) = 0$  do decrease significantly for solar metallicity fits.

Thus the very red objects in our fields appear to consist of two populations. The minority population has no dust and is red due to age and/or high metallicity, while the majority population is red due to dust, albeit with old age contributing to the red colors in some cases. This result may differ from those of Stiavelli & Treu (2000) and Moriondo, Cimatti, & Daddi (2000), who find that the fraction of dusty starbursts among VROs and EROs is  $\lesssim 30\%$  and  $\sim 20\%$ – $50\%$ , respectively, based on their morphologies as seen by *HST*. As discussed above, our heavily reddened objects and the irregular and exponential disk objects of Stiavelli & Treu (2000) and Moriondo, Cimatti, & Daddi (2000) may be different populations, but it would be very interesting if this discrepancy was real and indicated a breakdown in the relationship between morphology and star formation properties at  $z \gtrsim 1$ .

## 8. CONCLUSIONS

In previous work we have identified an excess population of predominantly red galaxies around a sample of 31 radio-loud quasars at  $1 < z < 2$ . In this paper we have presented new multiwavelength data and analyses on the fields of four of these quasars at  $z \sim 1.54$ , obtained to build more detailed pictures of the environments of these quasars and the galaxies within them. Our conclusions are as follows.

1. These fields have a surface density of extremely red objects (EROs, with  $R-K > 6$ ) 2.7 times higher than the general field. Assuming these EROs are passively evolved galaxies at the quasar redshifts, we find that they have characteristic luminosities of only  $\sim L^*$ . Thus these  $r-K$ -selected EROs are consistent with being drawn from the bright end of the luminosity function of early-type galaxies. The higher density of such EROs in RLQ fields can be easily understood if the RLQs are located in overdense regions. However, evolution in the dust content of these EROs could affect the luminosity estimates in up to  $\sim 40\%$  of the population. We also show that only one of four RLQ fields has an excess of  $J-K$ -selected EROs with  $J-K > 2.5$ . The majority of these EROs are therefore probably unrelated to the quasars.

2. Wide-field  $J$  and  $K_s$  data show that the galaxy excess around Q0835+580 extends to  $140''$  at  $2.35 \sigma$  significance, with a richness of  $N_{0.5} = 27 \pm 11$  (corresponding to Abell richness  $2 \pm 1$ ). The galaxy excess around Q1126+101 extends to only  $50''$ , suggesting that this quasar is embedded in a small-scale overdensity even though the overall counts in the field are higher than the literature average.

3. In three fields totaling  $10.156 \text{ arcmin}^2$  we present the deepest narrowband redshifted  $H\alpha$  observations published to date. We detect five candidate galaxies at the quasar redshifts, a surface density 2.5 times higher than in the only

existing random-field survey of similar depth. However, photometric SED fitting of one candidate suggests it is background to the quasar and that [O III]  $\lambda 5007$  instead of  $H\alpha$  was detected in the narrowband imaging.

4. Submillimeter observations of three fields with SCUBA detect two of the quasars and two galaxies whose SEDs are best fitted as highly reddened galaxies [ $E(B-V) \simeq 0.55$ ] at the quasar redshifts. While many galaxies whose SEDs indicate the presence of considerable dust are not detected, the SCUBA limits are only sufficient to rule out the hypothesis that these galaxies are hyperluminous infrared galaxies.

5.  $H$ -band adaptive optics imaging is used to estimate structural redshifts for two moderately red bulge-dominated galaxies in the Q0835+580 field using the Kormendy relation between central surface brightness and half-light radius. Both objects have structural redshifts consistent with ellipticals foreground to the quasar at  $z \lesssim 0.2$  or  $1 \lesssim z \lesssim 1.35$ . We have calculated photometric redshifts for these two objects for comparison with the structural redshifts. One object is not well fitted by any of the simple models we consider, whereas the other is only fitted by a moderately reddened and young galaxy at  $z_{\text{ph}} = 4.50 \pm 0.15$ . It seems likely that our optical photometry for these objects is corrupted by scattered light from the nearby bright star used for adaptive optics, resulting in inaccurate SED fits. Optical adaptive optics or *HST* imaging may be necessary to obtain accurate photometry for future study of these objects.

6. Quantitative SED fits and the resultant photometric redshifts are presented and discussed for numerous galaxies from specific populations of interest. Thirteen of eighteen objects in the spatially compact group around Q0835+580 are consistent with being at the quasar redshift at  $\gtrsim 90\%$  confidence. One of the thirteen is a candidate for a very old galaxy with no ongoing star formation; the others appear to have some ongoing star formation, as indicated by a best-fit constant star formation model or a young best-fit age. Fits to four  $J-K$ -selected EROs in the Q1126+101 field all require large reddenings of  $E(B-V) \simeq 0.6 \pm 0.3$ . One is consistent with the quasar redshift at 90% confidence, while the remaining three have best-fit photometric redshifts of  $1.9 < z_{\text{ph}} < 3$ . These objects may be indicative of a population of dusty, star-forming high-redshift galaxies potentially underrepresented in optically selected samples. Fits to 21 very or extremely red objects show that many of them have photometric redshifts consistent with the quasar redshifts. Significant dust is required to fit most of these objects, including about half of those which also require relatively old stellar populations.

Overall, our observations support the hypothesis that radio-loud quasars at  $z > 1$  can be found in galaxy overdensities. Among all but the very reddest galaxies in these overdensities, ongoing or recent star formation with moderate amounts of dust seems to be common. A similar result has been obtained by Yamada et al. (1997) for the galaxy excess around the RLQ 1335.8+2834 at  $z = 1.1$ , and a variation in recent star formation histories has also been suggested for the large-scale structures at  $z \sim 1.2$  in the field of 3C 324 (Kajisawa et al. 2000a). These results suggest that the  $z > 1$  redshift range is at least approaching the redshift range in which the majority of early-type cluster galaxies are undergoing significant bursts of star formation.

However, our finding that most very or extremely red objects require significant dust reddening may conflict with *HST* imaging results that show only  $\sim 20\%$ – $50\%$  of such objects have disklike or irregular morphologies suggestive of recent or ongoing star formation. This raises the intriguing possibility of a breakdown in the relationship between morphology and star formation properties at  $z \gtrsim 1$ . Spectroscopy will be needed to confirm these speculations, of course, and is needed in any case to confirm or calibrate our SED-fitting results.

We thank all our telescope operators and support astronomers, D. Thompson, and N. Drory for providing and discussing results prior to publication, P. Smith for IRTF observing help, and T. Pickering, T. Webb, A. Barger, M. Dickinson, and C. Kulesa for assorted help. Data were obtained (in part) using the 2.4 m Hiltner Telescope of the

MDM Observatory. TIFKAM was funded by the Ohio State University, the MDM consortium, MIT, and NSF grant AST-96 05012. NOAO and USNO paid for the development of the ALADDIN arrays and contributed the array in use in TIFKAM during our observations. M. S. acknowledges support from NSF grant AST-96 18686 and from the Natural Sciences and Engineering Research Council of Canada. R. A. F. acknowledges support from a UA/NASA Spacegrant Fellowship, NSF grant AST-96 23788, and NASA GSRP training grant NGT5-50283. H. L. acknowledges support provided by NASA through Hubble Fellowship grant HF-01110.01-98A awarded by the Space Telescope Science Institute, which is operated by the Association of Universities for Research in Astronomy, Inc., for NASA under contract NAS 5-26555. A. S. E. was supported by RF9736D.

## REFERENCES

- Barger, A. J., Cowie, L. L., Smail, I., Ivison, R. J., Blain, A. W., & Kneib, J.-P. 1999, *AJ*, 117, 2656
- Barkhouse, W. A., & Hall, P. B. 2001, *AJ*, in press
- Benítez, N., Broadhurst, T., Bouwens, R., Silk, J., & Rosati, P. 1999, *ApJ*, 515, L65
- Bruzual A., G., & Charlot, S. 1993, *ApJ*, 405, 538
- Bunker, A. J., Warren, S. J., Hewett, P. C., & Clements, D. L. 1995, *MNRAS*, 273, 513
- Burbidge, G., Hewitt, A., Narlikar, J. V., & Das Gupta, P. 1990, *ApJS*, 74, 675
- Calzetti, D. 1997, in *The Ultraviolet Universe at Low and High Redshift*, ed. W. H. Waller, M. N. Fanelli, & A. C. Danks (New York: AIP), 403
- Casali, M., & Hawarden, T. 1992, *JCMT-UKIRT Newsl.*, 4, 33
- Chapman, S. C., McCarthy, P., & Persson, S. E. 2000, *AJ*, 120, 1612
- Cimatti, A., Bianchi, S., Ferrara, A., & Giovanardi, C. 1997, *MNRAS*, 290, L43
- Cimatti, A., Daddi, E., di Serego Alighieri, S., Pozzetti, L., Mannucci, F., Renzini, A., Oliva, E., Zamorani, G., Andreani, P., & Röttgering, H. J. A. 1999, *A&A*, 352, L45
- Cimatti, A., Villani, D., Pozzetti, L., & di Serego Alighieri, S. 2000, *MNRAS*, 318, 453
- Cohen, J. G., Blandford, R., Hogg, D. W., Pahre, M. A., & Shopbell, P. L. 1999, *ApJ*, 512, 30
- Cohen, J. G., Hogg, D. W., Pahre, M. A., Blandford, R., & Shopbell, P. L. 1999, *ApJS*, 120, 171
- Coleman, G. D., Wu, C.-C., & Weedman, D. W. 1980, *ApJS*, 43, 393
- Cutri, R. M., Nelson, B. O., Kirkpatrick, J. D., Huchra, J. P., & Smith, P. S. 2000, in *ASP Conf. Ser.*, *The New Era of Wide-Field Astronomy*, ed. R. Clowes, A. Adamson, & G. Bromage (San Francisco: ASP), in press
- Daddi, E., Cimatti, A., Pozzetti, L., Hoekstra, H., Roettgering, H. J. A., Renzini, A., Zamorani, G., & Mannucci, F. 2000, *A&A*, 361, 535
- De Propriis, R., Eisenhardt, P. R., Stanford, S. A., & Dickinson, M. 1998, *ApJ*, 503, L45
- De Propriis, R., Stanford, S. A., Eisenhardt, P. R., Dickinson, M., & Elston, R. 1999, *AJ*, 118, 719
- Dey, A., Graham, J. R., Ivison, R. J., Smail, I., Wright, G. S., & Liu, M. C. 1999, *ApJ*, 519, 610
- Dey, A., Spinrad, H., & Dickinson, M. 1995, *ApJ*, 440, 515
- Drory, N., Hopp, U., Bender, R., Feulner, G., Snigula, J., Mendes de Oliveira, C., & Hill, G. 1999, in *ASP Conf. Ser.* 200, *Clustering at High Redshift*, ed. A. Mazure, O. Le Fevre, & V. LeBrun (San Francisco: ASP), 91 (D99)
- Dwek, E., et al. 1998, *ApJ*, 508, 106
- Eisenhardt, P. R., Armus, L., Hogg, D. W., Soifer, B. T., Neugebauer, G., & Werner, M. W. 1996, *ApJ*, 461, 72
- Eisenhardt, P. R., Elston, R., Stanford, S. A., Dickinson, M., Spinrad, H., Stern, D., & Dey, A. 2000, in *The Birth of Galaxies*, ed. B. Guiderdoni et al. (Gif-sur-Yvette: Ed. Frontières), in press
- Fioc, M., & Rocca-Volmerange, B. 1997, *A&A*, 326, 950
- Fukugita, M., Shimasaku, K., & Ichikawa, T. 1995, *PASP*, 107, 945
- Gardner, J. P., Sharples, R. M., Frenk, C. S., & Carrasco B. E. 1997, *ApJ*, 480, L99
- Gehrels, N. 1986, *ApJ*, 303, 336
- Girard, T. M., Grundy, W. M., López, C. E., & van Altena, W. F. 1989, *AJ*, 98, 227
- Graham, J. R., & Dey, A. 1996, *ApJ*, 471, 720
- Hall, P. B. 1998, Ph.D. thesis, Univ. Arizona
- Hall, P. B., & Green, R. F. 1998, *ApJ*, 507, 558 (HG98)
- Hall, P. B., Green, R. F., & Cohen, M. 1998, *ApJS*, 119, 1 (HGC98)
- Hall, P. B., Sawicki, M., & Lin, H. 2000, in *ASP Conf. Ser.* 200, *Clustering at High Redshift*, ed. A. Mazure, O. Le Fevre, & V. LeBrun (San Francisco: ASP), 205
- Hall, P. B., Sawicki, M., Pritchet, C. J., Hartwick, F. D. A., & Evans, A. 1999, in *ASP Conf. Ser.* 193, *The Hy-Redshift Universe: Galaxy Formation and Evolution at High Redshift*, ed. H. Spinrad, A. J. Bunker, & W. J. M. van Breugel (San Francisco: ASP), 415
- Hammer, F., Gruel, N., Thuan, T., Flores, H., & Infante, L. 2001, *ApJ*, in press
- Hill, G., & Lilly, S. 1991, *ApJ*, 367, 1
- Holland, W. S., Cunningham, C. R., Gear, W. K., Jenness, T., Laidlaw, K., Lightfoot, J. F., & Robson, E. I. 1998, *Proc. SPIE*, 3357, 305
- Hu, E. M., & Ridgway, S. E. 1994, *AJ*, 107, 1303
- Hunt, L. K., Mannucci, F., Testi, L., Migliorini, S., Stanga, R. M., Baffa, C., Lisi, F., & Vanzi, L. 1998, *AJ*, 115, 2594
- Jenness, T., & Lightfoot, J. F. 1998, *Starlink User Note* 216
- Kajisawa, M., et al. 2000a, *PASJ*, 52, 53
- . 2000b, *PASJ*, 52, 61
- Kennicutt, R. C. 1983, *ApJ*, 272, 54
- . 1998, *ARA&A*, 36, 189
- Kormendy, J., & Djorgovski, G. 1989, *ARA&A*, 27, 235
- Krisciunas, K., et al. 1987, *PASP*, 99, 887
- Leggett, S., & Denault, T. 1996, *NSFCAM 256 × 256 InSb Infrared Array Camera User's Guide*
- Leitherer, C. et al. 1996, *PASP*, 108, 996
- Liu, M. C., Dey, A., Graham, J. R., Bundy, K. A., Steidel, C. C., Adelberger, K., & Dickinson, M. E. 2000, *AJ*, 119, 2556
- Lin, H., et al. 2001, in preparation
- Martini, P. 2001, *AJ*, in press
- McCarthy, D. W., Ge, J., Hinz, J. L., Finn, R. A., & de Jong, R. S. 2000, *PASP*, submitted
- McCarthy, D. W., Ge, J., Hinz, J. L., Finn, R. A., Low, F. J., Cheselka, M., & Salvestrini, K. 1998, *BAAS*, 193, 11.09
- McCarthy, P. J., et al. 1999, *ApJ*, 520, 548
- Mendes de Oliveira, C., Drory, N., Hopp, U., Bender, R., & Saglia, R. P. 1998, *Wide Field Surveys in Cosmology*, ed. S. Colombi, Y. Mellier, & B. Raban (Gif-sur-Yvette: Ed. Frontières), 169
- Moriondo, G., & Cimatti, A., & Daddi, E. 2000, *A&A*, 364, 26
- Pahre, M. A., & Djorgovski, S. G. 1995, *ApJ*, 449, L1
- Persson, S. E., Murphy, D. C., Krzemiński, W., Roth, M., & Rieke, M. J. 1998, *AJ*, 116, 2475
- Pogge, R. W., et al. 1998, *SPIE*, 3354, 414
- Poggianti, B. M. 1997, *A&AS*, 122, 399
- Pozzetti, L., & Mannucci, F. 2000, *MNRAS*, 317, L17
- Pritchet, C. J., & Hartwick, F. D. A. 2001, in preparation
- Sánchez, S. F., & González-Serrano, J. I. 1999, *A&A*, 352, 383
- Sandage, A., & Perlmutter, J.-M. 1990, *ApJ*, 361, 1
- Saracco, P., D'Odorico, S., Moorwood, A., Buzzoni, A., Cuby, J.-G., & Lidman, C. 1999, *A&A*, 349, 751
- Sawicki, M., Lin, H., & Yee, H. K. C. 1997, *AJ*, 113, 1
- Sawicki, M., & Yee, H. K. C. 1998, *AJ*, 115, 1329
- Scodreggio, M., & Silva, D. R. 2000, *A&A*, 359, 953
- Smail, I., Ivison, R., Blain, A., & Kneib, J.-P. 1998, in *After The Dark Ages: When Galaxies Were Young*, ed. S. S. Holt & E. P. Smith (New York: AIP), 312
- Smail, I., et al. 1999, *MNRAS*, 308, 1061
- Soifer, B. T., Matthews, K., Neugebauer, G., Armus, L., Cohen, J. G., & Persson, S. E. 1999, *AJ*, 118, 2065
- Stanford, S. A., Elston, R., Eisenhardt, P. R., Spinrad, H., Stern, D., & Dey, A. 1997, *AJ*, 114, 2232
- Steidel, C. C., Giavalisco, M., Pettini, M., Dickinson, M., & Adelberger, K. L. 1996, *ApJ*, 462, L17
- Stiavelli, M., & Treu, T. 2000, in *ASP Conf. Ser.*, *Galaxy Disks and Disk Galaxies*, ed. J. G. Funes, & E. M. Corsini (San Francisco: ASP), in press
- Teplitz, H., McLean, I., & Malkan, M. 1999, *ApJ*, 520, 469

- Thompson, D., Afreth, O., & Soifer, B. T. 2000, *AJ*, 120, 2331
- Thompson, D., Kelly, A. E., Sawicki, M., Soifer, B. T., & Matthews, K. 1999, in *ASP Conf. Ser. 191, Photometric Redshifts and High Redshift Galaxies*, ed. R. Weymann, L. Storrie-Lombardi, M. Sawicki, & R. Brunner (San Francisco: ASP), 291
- Thompson, D., et al. 1999, *ApJ*, 523, 100 (T99)
- Thompson, R., Weymann, R., & Storrie-Lombardi, L. 2000, *ApJ*, 546, 694
- Tytler, D., & Fan, X.-M. 1992, *ApJS*, 79, 1
- Valdes, F. 1982, *FOCAS User's Manual*
- van Breugel, W. J. M., De Breuck, C., Stanford, S. A., Stern, D., Röttgering, H., & Miley, G. 1999, *ApJ*, 518, L61
- van Breugel, W. J. M., Stanford, S. A., Spinrad, H., Stern, D., & Graham, J. R. 1998, *ApJ*, 502, 614
- van der Werf, P. P. 1997, in *Extragalactic Astronomy in the Infrared*, ed. G. A. Mamon, T. X. Thuan, & Trần Thanh Vân (Gif-sur-Yvette: Ed. Frontières), 451
- Yamada, T., Tanaka, I., Aragon-Salamanca, A., Kodama, T., Ohta, K., & Arimoto, N. 1997, *ApJ*, 487, L125
- Yee, H. K. C. 2000, in *The Birth of Galaxies*, ed. B. Guideroni, F. R. Bouchet, T. X. Thuan, & J. Trần Thanh Vân (Gif-sur-Yvette: Ed. Frontières)
- Yee, H. K. C., & Ellingson, E. 1993, *ApJ*, 411, 43